TECHNISCHE UNIVERSITÄT WIEN

DISSERTATION

A constitutive model for fiber reinforced plies – Anisotropic evolution of damage and plasticity

ausgeführt zum Zwecke der Erlangung des akademischen Grades eines
Doktors der technischen Wissenschaften unter der Leitung von

Assoc.Prof. Dipl.-Ing. Dr.techn. Heinz Pettermann

E317

Institut für Leichtbau und Struktur-Biomechanik

eingereicht an der Technischen Universität Wien
Fakultät für Maschinenwesen und Betriebswissenschaften

von

Jan Kaul, MSc

Matrikelnummer 01647179

Liniengasse 9/4

1060 Wien

Wien, im Juli 2020   Jan Kaul

Affidavit

I declare in lieu of oath, that I wrote this thesis and performed the associated research myself, using only literature cited in this volume. If text passages from sources are used literally, they are marked as such. I confirm that this work is original and has not been submitted elsewhere for any examination, nor is it currently under consideration for a thesis elsewhere.

Vienna, Juli 2020

_____

Jan Kaul

Abstract

Due to their heterogeneous microstructure, laminates made of fiber reinforced polymers (FRP) show different failure modes. Some failure modes, such as fiber damage, are critical to the integrity of the laminate and some failure modes, such as inter-fiber failure, do not lead to immediate failure. To further exploit the exceptional weight-specific material properties of FRPs, inter-fiber failure gets tolerated to some extent. However, numerical analysis tools are required to assure the safety of FRP components.

The main goal of the present thesis is to provide a constitutive model that can be used with the Finite Element Solver ABAQUS/Standard 2019 (SIMULIA, Providence, RI, USA) to give reliable predictions concerning fiber damage, inter-fiber damage and plastic yielding in FRP plies. To be useful for a general engineer, the model shall (1) be calibrated with standard experiments and (2) use a robust and efficient solution algorithm.

The proposed constitutive model combines an explicit damage model for fiber fracture, an implicit damage model for inter-fiber fracture, and a plasticity model for unrecoverable strains. The implicit damage model for inter-fiber failure is based on a constraint problem and allows for an anisotropic evolution of the damage condition. This is achieved by introducing multiple loading-threshold functions that directly depend on the damage variables. The loading-threshold functions are set up to reproduce experimental stress-strain curves for in-plane shear, uni-axial transverse tension, and uni-axial transverse compression. The model derives the damage flow rule from the Puck failure criterion and can distinguish between different inter-fiber failure modes, which can indicate whether the damage is tolerable or critical for the laminate. To combine the damage formulation with plasticity, the damage condition is formulated in terms of effective variables, as defined in Continuum Damage Mechanics. This way the evolution equations for plasticity are independent of damage. The plasticity formulation is set up to model combined isotropic and

kinematic hardening behavior and allows for different behaviors under in-plane transverse compression and in-plane shear.

To assess the predictive capabilities of the constitutive model, its predictions are computed for three applications. The results show that the constitutive model can predict plastic yielding with kinematic hardening behavior and inter-fiber failure for FRP structures. Moreover, the numerical solution procedure of the constitutive model is robust and efficient enough to perform structural computations with reasonable computational effort.

Kurzfassung

Laminate aus faserverstärkten Polymeren (FRP) weisen aufgrund ihrer heterogenen Mikrostruktur unterschiedliche Versagensarten auf. Einige Versagensarten, wie z. B. der Faserbruch, sind kritisch für den Zusammenhalt des Laminats, und einige Versagensarten, wie z. B. der Zwischenfaserbruch, führen nicht zu einem sofortigen Versagen. Um die außergewöhnlichen gewichtsspezifischen Materialeigenschaften von FRPs weiter auszunutzen, wird der Zwischenfaserbruch bis zu einem gewissen Grad toleriert. Es sind jedoch numerische Analysewerkzeuge erforderlich, um die Sicherheit von FRP-Komponenten zu gewährleisten.

Das Hauptziel der vorliegenden Arbeit ist es, ein Konstitutivgesetz bereitzustellen, das mit dem Finite Elemente Solver ABAQUS / - Standard 2019 (SIMULIA, Providence, RI, USA) verwendet werden kann, um verlässliche Vorhersagen über Faserbruch, Zwischenfaserbruch und plastiches Fließen in FRP Laminaten zu treffen. Um für einen allgemeinen Ingenieur nützlich zu sein, muss das Modell (1) mit Standardexperimenten kalibrierbar sein und (2) einen robusten und effizienten Lösungsalgorithmus verwenden.

Das vorgeschlagene Konstitutivgesetz kombiniert ein explizites Schädigunsmodell für Faserbruch, ein implizites Schädigungsmodell für Zwischenfaserbruch und ein Plastizitätsmodell für plastische Dehnungen. Das implizite Schädigunsmodell für Zwischenfaserbruch verwendet zusätzliche Nebenbedingungen und ermöglicht eine anisotrope Entwicklung der Schädigungsbedingung. Dies wird durch die Einführung mehrerer "Loading-threshold" Funktionen erreicht, die direkt von den Schädigungsvariablen abhängen. Die "Loading-threshold" Funktionen sind so definiert, dass Sie experimentelle Spannungs-Dehnungs-Kurven für Scherung, einachsige Quer-Zugbelastung und einachsige Quer-Druckbelastung reproduzieren können. Das Modell leitet die Schädigungs-Fließregel aus dem Puck-Versagenskriterium ab und kann zwischen verschiedenen Versagensmodi unterscheiden, die

andeuten können, ob der Schaden für das Laminat tolerierbar oder kritisch ist. Um die Schädiguns- mit der Plastizitätsformulierung zu kombinieren, wird die Schädigungsbedingung in Abhängigkeit von effektiven Variablen formuliert, wie sie in Continuum Damage Mechanics definiert sind. Auf diese Weise sind die Evolutionsgleichungen für die Plastizität unabhängig von der Schädigung. Die Plastizitätsformulierung ist so aufgebaut, dass sie kombinierte isotrope und kinematische Verfestigung modelliert und unterschiedliche Verhaltensweisen bei Querkompression und Scherung ermöglicht.

Um die Vorhersagefähigkeit des Konstitutivgesetzes zu bewerten, werden seine Vorhersagen für drei Anwendungen berechnet. Die Ergebnisse zeigen, dass das Konstitutivgesetz plastische Dehnungen mit kinematischem Verfestigungsverhalten und Zwischenfaserbruch für FRP-Strukturen vorhersagen kann. Darüber hinaus ist das numerische Lösungsverfahren des Konstitutivgesetzes robust und effizient genug, um Strukturberechnungen mit angemessenem Rechenaufwand durchzuführen.

Contents

V

Acknowledgment

First of all, I would like to express my deepest gratitude to my thesis advisor Assoc. Prof. Dr. H. Pettermann for his guidance and support during my doctorate studies. He would always ask me the right questions that helped me consolidate my ideas and made sure I wasn't missing the "bigger picture".

Additionally, I would like to thank my office colleagues Tilen Ceglar, Dr. Benjamin Werner, Jaques Zwar, and Martin Springer for always providing valuable distractions during our coffee breaks. I consider myself extremely lucky to have had colleagues that share the same (silly) humor and interests.

Generally, I would like to thank all members of the ILSB for creating such a friendly and supportive work environment. In particular, I thank Maria Steininger for all the administrative help and Gerhard Schneider for providing an exceptional IT infrastructure.

Last but not least, I would like to thank my friends and family, who supported me even at times when I didn't have as much time for them as I wanted.

Notation

Scalar variables

Ψ .... Helmholtz free energy density

Ψ^{e} .... Elastically stored free energy density

Ψ_0^{p} .... Effective plastic free energy density

d_1 .... Fiber damage variable

d_2 .... Inter-fiber damage variable associated with cracks perpendicular to the ply plane

d_3 .... Inter-fiber damage variable associated with inclined cracks

d_1^{v} .... Viscous fiber damage variable

d_2^{v} .. Viscous inter-fiber damage variable associated with cracks perpendicular to the ply plane

d_3^{v} .... Viscous inter-fiber damage variable associated with inclined cracks

ζ_1 .... Fiber inelastic compliance variable

ζ_2 .. Inter-fiber inelastic compliance variable associated with cracks perpendicular to the ply plane

ζ_3 .... Inter-fiber inelastic compliance variable associated with inclined cracks

$\zeta_2^{\mathrm{T, \, c}}$ Critical inelastic compliance variable ζ_2 for softening onset under transverse tension

$\zeta_3^{\mathrm{C, \, c}}$ .... Critical inelastic compliance variable ζ_3 for softening onset under transverse compression

$\zeta_2^{\mathrm{S, \, c}}$ ... Critical inelastic compliance variable ζ_2 for softening onset under in-plane shear

$\tilde{a}_1$ .... Transverse compressive hardening variable

$\tilde{a}_2$ .... In-plane shear hardening variable

$\tilde{a}_1^{(3)}$ .... Transverse compressive hardening variable at softening onset

$\tilde{a}_2^{(3)}$ .... In-plane shear hardening variable at softening onset

R_1 .... Current transverse tensile strength

R_2 .... Current transverse compressive strength

R_3 .... Current in-plane shear strength

$\tilde{R}_1$ .... Loading threshold function for transverse tension

$\tilde{R}_2$ .... Loading threshold function for transverse compression

$\tilde{R}_3$ .... Loading threshold function for in-plane shear

$\mathcal{D}$ .... Dissipation

E_1 .... Longitudinal Young's modulus

E_2 .... Transverse Young's modulus

G_{12} .... In-plane shear modulus

G_{23} .... Out-of-plane shear modulus

ν_{12} .... In-plane poission ratio

X^{T} .... Longitudinal tensile strength

X^{C} .... Longitudinal compressive strength

$\mathcal{G}^{\mathrm{F,\,T}}$ .... Longitudinal tensile fracture energy

$\mathcal{G}^{\mathrm{F,\,C}}$ ....Longitudinal compressive fracture energy

Y_0^{T} .... Initial plasticity threshold under transverse tension

Y_1^{T} .... Initial damage threshold under transverse tension

Y_2^{T} .... Transverse ultimate tensile strength

$\tilde{Y}_3^{\mathrm{T}}$ .... Effective ultimate transverse tensile strength

Y_0^{C} .... Initial plasticity threshold under transverse compression

Y_1^{C} .... Initial damage threshold under transverse compression

Y_2^{C} .... Transverse ultimate compressive strength

$\tilde{Y}_3^{\mathrm{C}}$ .... Effective ultimate transverse compressive strength

S_0 .... Initial plasticity threshold under in-plane shear

S_1 .... Initial damage threshold under in-plane shear

S_2 .... Ultimate shear strength

$\tilde{S}_3$ .... Effective ultimate shear strength

$\mathcal{G}^{\mathrm{M,\,T}}$ .... Transverse tensile fracture energy

$\mathcal{G}^{\mathrm{M,\,C}}$ .... Transverse compressive fracture energy

$\mathcal{G}^{\mathrm{M,\,S}}$ .... In-plane shear fracture energy

c_1^{p} .... Plasticity parameter for compression

c_2^{p} .... Plasticity parameter for shear

p^{T} .... Puck slope parameter for tension

p^{C} .... Puck slope parameter for compression

η .... Viscous regularization parameter

C^T .... Fitting parameter for transverse tension

C^C .... Fitting parameter for transverse compression

C^S .... Fitting parameter for in-plane shear

W .... Elastically stored energy from the unloaded state until softening onset

W^{T} ....Elastically stored energy from the unloaded state until softening onset for transverse tension

W^{C} ....Elastically stored energy from the unloaded state until softening onset for transverse compression

W^{S} . Elastically stored energy from the unloaded state until softening onset for in-plane shear

L^{e} .... Characteristic element length

$F_{\mathrm{d}}^{\mathrm{F}}$ .... Fiber damage condition

$F_{\mathrm{d}}^{\mathrm{M}}$ .... Inter-fiber damage condition

F_{p} .... Yield condition

λ_{d} .... Damage multiplier

λ_{p} .... Plasticity multiplier

θ .... Puck fracture angle

θ_{max} .... Maximum Puck fracture angle

R^{A} .... Fracture resistance of the Puck action plane

τ^{c} .... Critical shear stress for Mode C fracture

$\tilde{\mathcal{D}}_{\mathrm{p}}$ .... Effective plastic dissipation

α .... Isotropic/Kinemataic hardening parameter

E^{M} .... Young's modulus of the matrix material of the fabric laminated structure

ν^{M} .... Poisson ratio of the matrix material of the fabric laminated structure

$R_{\mathrm{y}}^{\mathrm{M}}$ .... Initial yield strength of the matrix material of the fabric laminated structure

R^{M} ....Ultimate strength of the matrix material of the fabric laminated structure

$\mathcal{G}^{\mathrm{M}}$ .... Fracture energy of the matrix material of the fabric laminated structure

Vectors

$\mathbf{d}$ ....Vector of damage variables

$\mathbf{Y}$ ....Vector of associated thermodynamic forces for the damage variables

$\tilde{\mathbf{a}}$ ....Vector of effective hardening variables

$\tilde{\mathbf{A}}$ ......Vector of associated thermodynamic forces for the effective hardening variables

$\mathbf{D}$ ....Damage direction vector

Second order tensors

$\boldsymbol{\varepsilon}$ ....Total strain tensor

$\boldsymbol{\varepsilon}^{\mathrm{e}}$ ....Elastic strain tensor

$\boldsymbol{\varepsilon}^{\mathrm{p}}$ ....Plastic strain tensor

$\tilde{\boldsymbol{\varepsilon}}^{\mathrm{e}}$ ....Effective elastic strain tensor

$\tilde{\boldsymbol{\varepsilon}}^{\mathrm{p}}$ ....Effective plastic strain tensor

$\boldsymbol{\sigma}$ ....Stress tensor

$\tilde{\boldsymbol{\sigma}}$ ....Effective stress tensor

$\boldsymbol{\varepsilon}_{\mathrm{c}}^{\mathrm{e}}$ ....Elastic strain tensor at softening onset

$\boldsymbol{\sigma}_{\mathrm{c}}$ ....Stress tensor at softening onset

$\boldsymbol{\varepsilon}_{\infty}^{\mathrm{e}}$ ....Elastic strain tensor at total failure

$\boldsymbol{\sigma}_{\infty}$ ....Stress tensor at total failure

Fourth order tensors

$\mathbb{C}$ ....Compliance tensor

$\mathbb{C}^{(0)}$ ....Undamaged compliance tensor

$\mathbb{E}^{(0)}$ ....Undamaged elasticity tensor

$\mathbb{I}$ ....Fourth order symmetric identity tensor

$\mathbb{D}^{(1)}$ ....Damage contribution tensor for damage variable d_1

$\mathbb{D}^{(2)}$ ....Damage contribution tensor for damage variable d_2

$\mathbb{D}^{(3)}$ ....Damage contribution tensor for damage variable d_3

$\mathbb{M}$ ....Damage effect tensor

$\mathbb{M}_\mathrm{c}$ ....Damage effect tensor at softening onset

$\mathbb{M}_\infty$ ....Damage effect tensor at total failure

$\mathbb{S}$ ....Eshelby tensor

Operators

$\cdot$ ......Inner product (full contraction of both operands), i.e. $\mathbf{a} \cdot \mathbf{b} = a_i b_i$, $\boldsymbol{\sigma} \cdot \boldsymbol{\varepsilon} = \sigma_{ij}\varepsilon_{ij}$

$\otimes$ ....Dyadic product, i.e. $\mathbf{a} \otimes \mathbf{b} = a_i b_j$, $\boldsymbol{\sigma} \otimes \boldsymbol{\varepsilon} = \sigma_{ij}\varepsilon_{kl}$

$||$ ....Magnitude

$\langle\;\rangle$ ....Macauley operator

Chapter 1

Introduction

Due to their high weight-specific stiffness and strength, laminates made of fiber-reinforced polymers (FRPs) are becoming increasingly popular in high-performance applications. Besides their use for wind turbines, automobiles, and sports equipment, they are used increasingly in aerospace industries. Due to the rising crude oil prices over the last 20 years, aircraft manufactures were driven to develop lighter and more fuel-efficient aircraft. This has lead to an increased usage of structural FRP components in recent aircraft designs. The Airbus 380, which was introduced into the market in 2005, is made of 20% composite materials. The newest generation of large passenger aircraft, like the Boeing 787 Dreamliner or the Airbus A350 XWB, consist of 50% composite materials. Whether the trend continues is unknown and depends on the cost-efficiency of the FRP design and manufacturing process.

The excellent properties of FRP structures come from the reinforcement fibers that have very high stiffness and strength. For most applications either carbon, glass, or aramid fibers are used. Since the fibers can only transfer tensile loads, they are embedded in matrix material, which enables a load transfer between the fibers. The matrix material is typically made of either thermosets (e.g. epoxy, polyester) or thermoplastic polymers (e.g. polyamide). The fibers and the matrix material can be used in different arrangements depending on the application. For high-performance applications, they are deployed as laminates of unidirectional reinforced plies, whose mechanical properties are strongly direction-dependent. To use the reinforcement effect in multiple directions, the plies are stacked with different orientations. This way the laminate stacking can be

tailored according to the application.

Due to the topology of FRPs laminates, they possess several failure modes. The failure modes can be distinguished into the failure between the plies, called interlaminar failure, and the failure in the ply, called intralaminar failure. Interlaminar failure occurs in the form of decohesion at the interface between two adjacent plies. At the interface, there is no reinforcement of the fibers, making it a weak point. Interlaminar failure also referred to as delamination, is often caused by stress concentrations in the vicinity of free-edges or close to intralaminar failure. The result is a crack that develops in the interface and that can be driven by static or cyclic loading. Intralaminar failure occurs either as fiber fracture, matrix fracture, or fiber-matrix debonding. Due to the high fracture toughness of the fibers, fiber fracture typically leads to the failure of the whole laminate. Matrix fracture and fiber-matrix debonding, often treated together as inter-fiber failure, on the other hand, can be tolerated to some extent. If inter-fiber failure occurs, the load is redistributed in the laminate without causing fiber fracture in the surrounding plies.

Due to their complex failure, FRPs come at a high cost for their design and manufacturing. To compete with conventional materials, their full potential has to be utilized. This can be achieved by tolerating the failure mechanisms, that do not lead to immediate structural failure, i.e. inter-fiber failure. Structural FRP components can typically withstand a load increase after the initial onset of inter-fiber failure. It is critical however, that the different failure modes can be distinguished and that the response after initial failure can be predicted. This is a challenge for the design of FRP structures and requires advanced numerical simulations to make reliable predictions. The scope of the present work is to develop a tool that can predict intralaminar failure of FRPs and that can be used with the Finite Element Method (FEM) to assist in the design process of FRP structures. The present work is organized as follows.

Chapter 1.1 reviews the existing literature and summarizes the approaches that have been developed to predict the failure of FRPs. A special focus lies on the anisotropic damage models that are used to describe the stiffness degradation related to intralaminar failure. Additionally, contributions to modeling plastic yielding of FRPs are reviewed.

Based on the observations regarding the existing literature, Chapter 1.2 formulates the main aim of the thesis and discusses different aspects of it.

Chapter 2 introduces ply modeling to cope with the complexity that arises from the different length scales that are present in FRP laminates. Additionally, the different failure modes of individual FRP plies are presented.

Chapter 3 presents the constitutive model. The model is presented in terms of its internal state variables that are used to model the occurring phenomena, followed by the criteria and equations for their evolution.

To use the constitutive model in numerical computations, Chapter 4 presents the algorithm that is used for the implementation of the model. The first part focuses on the constitutive integration algorithm that solves the governing evolution equations. The second part shows the algorithmic consistent material tangent matrix that is required by the Newton-Solver that is typically used to solve the nonlinear system of equations produced by the FEM.

Chapter 5 is a collection of applications that are performed to highlight different capabilities of the proposed constitutive model. The first application aims at the plasticity formulation, especially the prediction of the kinematic hardening behavior that can occur during cyclic loading. The second application is to highlight the predictions for plasticity and damage on structural components. The third application applies the constitutive model to model the response of the tows inside a fabric structure.

1.1 Literature review

1.1.1 Modeling of Intralaminar failure

The different forms of intralaminar failure, namely fiber failure, fiber-matrix debonding, and matrix failure, all lead to a separation of the material. As a consequence, intralaminar failure can be regarded as a fracture problem. Typically fracture is modeled with either discrete or continuous models.

In discrete models, the crack is modeled as a discrete entity whose position has to be captured by the description of the displacement field. This can be done by making sure that the FEM mesh has nodes at the position of the crack or by enhancing the displacement field with a displacement jump. For the former approach a standard FEM implementation can be used but frequent remeshing is required when the crack propagates. For the latter approach the displacement field needs to be enhanced by employing the extended-Finite-Element Method [4] or the Phantom-Node Method [41]. In addition to the geometrical description of the crack, criteria for initiation, propagation, and orientation of the crack are required. The propagation of the crack is often modeled by Linear-Elastic-Fracture-Mechanics (LEFM) or by the cohesive zone model developed by Dugdale [7] and Barenblatt [2].

Continuous models treat fracture within the constitutive model for the bulk material. This is typically done by employing Continuum-Damage-Mechanics (CDM). CDM has been proposed in [22] for isotropic damage and has been extended to anisotropic damage in several ways. The anisotropic damage models can be categorized into ones with explicit damage evolution laws and ones with implicit damage evolutions defined as a constraint problem. The majority of damage models for FRPs use explicit damage evolution laws but use different approaches on how the damage variables affect the stiffness degradation. The anisotropic damage models proposed in [26, 29, 28] introduce damage variables where one damage variable reduces one engineering modulus of the material. Therefore, a single damage variable affects only its corresponding entry in the compliance tensor. In some cases, for example for damage under normal and shear loading, it is desired that one damage variable affects multiple entries in the compliance tensor. To affect multiple entries in the compliance tensor, the damage models proposed in [44, 27, 36, 35] express

certain secondary damage variables as functions of multiple primary damage variables. This way the entries in the compliance tensor formulated in terms of the secondary damage variables are affected by the primary damage variables. This captures the interaction but it only works in one direction. The damage under normal loading affects the shear damage, but not vice versa. Another way to affect multiple entries in the compliance tensor is to base the damage effect on micro-mechanical considerations. The benefit is that the relations between different entries in the compliance tensor are not defined through approximate formulas but are motivated through micro-mechanical reasoning. Micro-mechanically motivated damage models with explicit damage evolution laws have been proposed in [37, 10, 11, 39]. Explicit damage evolution laws are calibrated with one stress-strain curve per damage variable. This leads to very efficient computations, but the evolution of a damage variable, which affects multiple engineering moduli, can only be calibrated correctly for one. It is not possible to prescribe the normal and shear behavior independently, if the damage variable affects the corresponding Young's and shear modulus.

The second category of damage evolutions is calculated implicitly through a constraint problem, defined by a damage condition and a damage flow rule. The models proposed in [6, 8] formulate the constraint problem in terms of the associated thermodynamic forces of the damage variables, which can be considered as energy release rates. The solution is obtained by maximizing the dissipation under the constraint of satisfying the damage condition. The energy release rates can be related to fracture mechanics and are typically used to model brittle materials. For FRPs it is desired to have strength-based damage conditions because the established failure criteria proposed in [34, 33] can be used. The models proposed in [16, 19, 45, 18] use strength-based damage conditions. They introduce loading-threshold functions that govern the evolution of the damage condition. Since the number of loading-threshold functions is not tied to the number of damage variables, an arbitrary number of functions can be defined for the damage evolution. Consequently, the evolution of one damage variable, that affects multiple entries in the compliance tensor, can be prescribed to comply with multiple experimental curves. The difficulty lies in formulating the dependence of the loading-threshold functions on the internal state variables. To overcome this, the aforementioned models introduce an additional internal state

variable whose associated thermodynamic force is used as a loading-threshold function. However, using only one state variable and one loading-threshold function allows only an isotropic evolution of the damage condition. To prescribe different evolutions of the damage condition under different loads, it is desired to have multiple loading-threshold functions, that can be calibrated independently.

1.1.2 Modeling of plastic yielding in fiber reinforced polymers

For angle- and cross-ply laminates, inter-fiber fracture can be accompanied by the accumulation of unrecoverable strains. Such laminates can obtain a higher weight-specific strength and stiffness in predefined directions than quasi-isotropic laminates but are more susceptible to matrix related phenomena. To predict the response of such laminates accurately, it is shown in [5] that it is important to model the nonlinear behavior due to the unrecoverable strains. The plasticity models that are employed to model the unrecoverable strains use yield functions that are either formulated in terms of selected stress components or in terms of transversely isotropic stress invariants. For triaxial stress states the use of stress invariants is beneficial because it reduces the number of variables and leads to a more physical decomposition of the stress tensor. Plasticity models for FRPs that use transversely isotropic stress invariants have been developed in [30, 42, 32]. The model from [30] assumes associative yielding. However, it is stated in [42] that associative yielding can lead to wrong predictions for the volumetric plastic strain for FRPs. As a remedy, a non-associative flow rule is proposed in [42]. The model from [32] proposes a non-associative plasticity model that uses the yield function as flow potential except that it neglects the stress in fiber direction and the hydrostatic pressure.

For many applications of FRP components, a plane stress state can be assumed. As a result, there are not many non-zero stress components, such that the use of invariants is not needed. The plane stress plasticity model developed in [40] has the benefit compared to triaxial models that only two parameters have to be calibrated. In [26] the same yield surface is used to combine plasticity with damage.

Another plane stress plasticity model is proposed in [10], where two independent plasticity formulations are used for the plastic yielding under in-plane shear and transverse compression.

1.2 Aims and Objective

The main aim of the thesis is to provide a tool that can be used by engineers to obtain reliable predictions regarding the failure of laminated FRP structures. Since there is a large variety of FRP materials, which cannot all be considered, the present work focuses on thermoset polymers reinforced with carbon or glass fibers. As a consequence, the most relevant failure mechanisms are fiber fracture, inter-fiber fracture, and the accumulation of unrecoverable strains. Viscoelastic and -plastic behavior shall not be considered. The main aim can be decomposed into several aspects.

Most importantly, the developed tool should be usable by a general engineer. Consequently, the failure of FRPs shall be predicted by a constitutive model that can be used with standard FEM software. Besides, only material parameters shall be used that can be obtained from standard experiments.

Another aspect is to provide reliable predictions that are valid for arbitrary loading without the need to recalibrate. To achieve this, the objective is to use a micromechanically motivated damage formulation. Thereby, multiple engineering moduli are degraded by one kind of damage, which closely resembles the actual physical phenomenon. Additionally, an implicit damage formulation shall be used, such that the evolution of one kind of damage can be calibrated to different kinds of loading.

The constitutive model has to meet certain robustness and efficiency requirements when applied to structural components. To achieve these requirements without compromising its predictive capabilities, the model is developed with the following additional objectives. First, the damage condition and the loading threshold functions shall be formulated in terms of the effective stresses as opposed to the nominal stresses. This way the loading threshold functions are injective functions in terms of the damage variable for both hardening and softening, which increases the robustness of the solution procedure. Second, the principle of elastic strain equivalence shall be used because it simplifies the calculation of the effective stress, which increases the numerical efficiency of the model. Third, two independent formulations for damage and plasticity shall be used because it simplifies the solution procedure.

Chapter 2

Fiber-reinforced polymers

In the following the structure and the failure modes of FRP laminates are introduced as a basis for the derivation of the constitutive equations. First, a modelling approach for the structure of unidirectionally reinforced laminates is presented. Second, the different failure modes occurring in unidirecitonal FRP laminates are shown.

2.1 Length-scales

The failure of FRP components is significantly influenced by the geometry and the arrangement of its constituents. Of highest interest are those arrangements that lead to the highest stiffness and strength. The highest stiffness and strength can be reached when the fibers are aligned as straight as possible. As a consequence, this work concerns itself with laminates of unidirectional fiber-reinforced plies. The structure of such laminates shows several characteristic length scales. On one side, there is the diameter of the fibers which is typically around 10 μm. The fiber diameter characterizes the behavior of the microstructure. This scale is typically referred to as the micro-scale (Figure 2.1a). It is at that scale where the matrix material transfers the stresses between the fibers.

Another characteristic length of the laminate structure is the thickness of a ply, which is around 0.1 − 0.2 mm. This scale is called the mesoscale (Figure 2.1b). Depending on the application, the plies are stacked with different orientations. One reason for that is that the laminate has higher stiffness and strength in multiple directions. Besides, it is helpful to stack adjacent plies with different orientations because the fracture that might

(a)   (b)   (c)
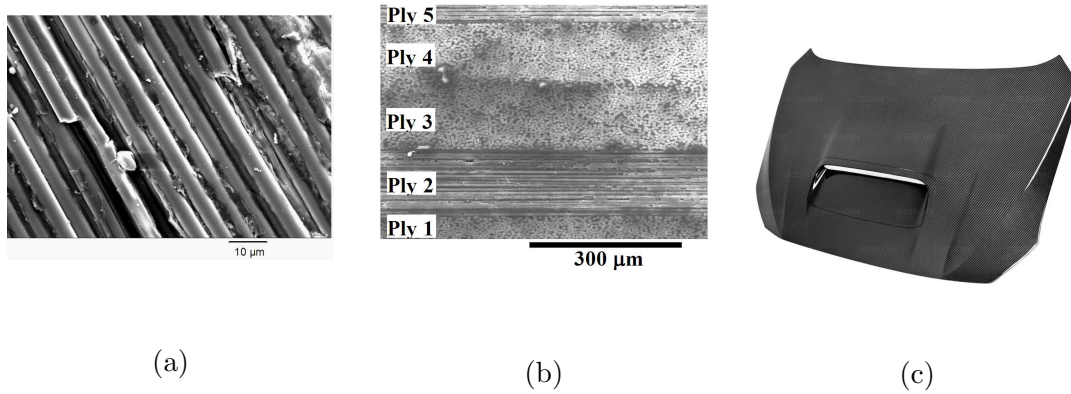
Figure 2.1: Characteristic length scales than can be observed in UD-reinforced fiber-reinforced poymer laminates; Composed of the micro-scale (a) [14], meso-scale (b) [14] and the macro-scale (c) [1].

occur in one ply is more likely to be stopped by a ply with a different orientation. If a plane loading is expected, a homogeneous stacking of the plies can be beneficial. This means that plies with the same orientation are evenly distributed over the thickness of the laminate. Another important aspect is to use a symmetrical stacking sequence with respect to the middle-plane of the laminate. This way, wrinkling due to mechanical or thermal loading can be prevented.

The largest scale is the macro-scale (Figure 2.1c), which is equal to the dimensions of the component. At this scale the boundary conditions and loads are applied to the component.

For the numerical analysis, it is not feasible to account for all scales explicitly. To simplify the modeling, this work employs a phenomenological approach at the mesoscale. Therefore, each ply is modeled with homogeneous material behavior. However, certain characteristics of the micro-structure are used to derive the phenomenological formulations for the mesoscale.

2.2 Failure of fiber reinforced polymer plies

Fiber reinforced polymers show different failure modes due to their heterogeneous microstructure. It is important to distinguish these different failure modes to prevent critical modes in the design process. In this context, failure means the complete separation of the material due to mechanical loads. However, there are different kinds of mechanical loads that lead to failure, i.e. fatigue, dynamic, and static loads. The individual resistances against these loads have to be determined experimentally. In the present work, the focus is on static or quasi-static loads. The strength analysis of laminates of FRPs is typically performed at the ply level and the ply deformation is obtained from the laminate deformation either through laminate theory or numerical methods.

Fiber fracture. In this context, fiber fracture means the breakage of a bundle of fibers, not just individual fibers. The result is the loss of load bearing capacity of the ply in the fiber direction. Due to their high stiffness in the fiber direction, the fibers are mainly loaded by the longitudinal stress. The other stress components are significantly smaller because they also have to be sustained by the matrix material. As a consequence, fiber fracture occurs either through longitudinal tensile or compressive stresses. Under tensile loads, fibers rupture occurs, which is depicted in Figure 2.2a. The stress-strain behavior is linear until rupture. Compressive longitudinal stresses lead to fiber kinking or micro-buckling, which occurs when the necessary elastic support of the matrix material is exceeded. Fiber kinking typically localizes into kink-bands, which is depicted in Figure 2.2b. Fiber failure usually also leads to matrix failure, because the released energy is too high that it can be redistributed in the surrounding material. The result is macroscopic fracture that leads to structural failure.

Inter fiber fracture. Inter fiber fracture occurs as cracks in the matrix material or at the fiber-matrix interface. The cracks run through the whole thickness of a ply and are only stopped by the fibers of the adjacent plies. An exemplary crack is shown in Figure 2.3. Inter fiber fracture leads to a redistribution of stresses inside a laminate. The load gets reintroduced into the broken ply through shear stresses at a certain distance from the crack. Macroscopically, the broken ply can be regarded as a continuum with degraded
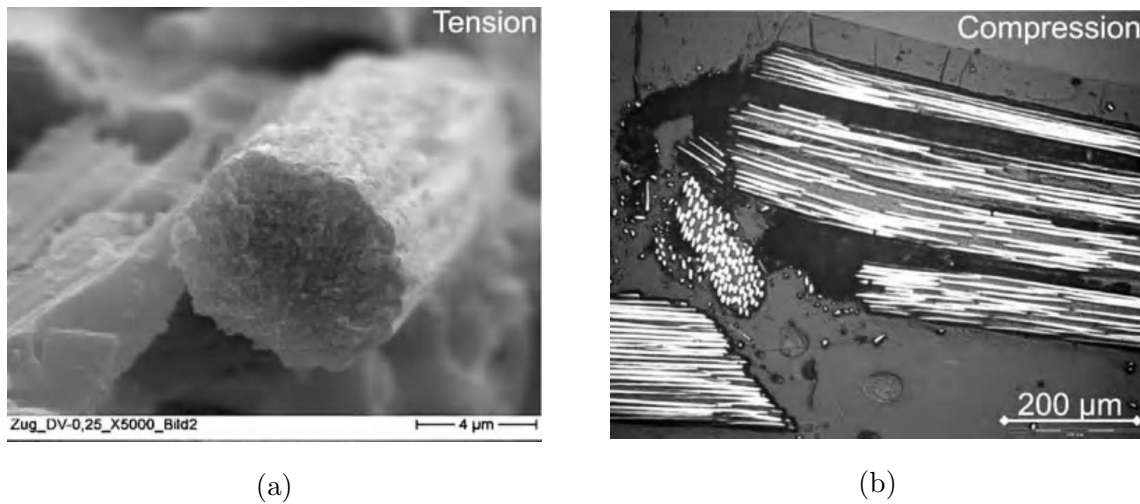
(a)

(b)

Figure 2.2: Pictures of fiber rupture under tension (a) and fiber kinking (b) for the carbon fibers T300 [25].

stiffness. If the load is increased, further matrix-cracks will be initiated. When a critical load is reached, the delamination of the interfaces adjacent to the broken ply will grow and the ply can eventually be pulled out. Matrix cracks are oriented parallel to fibers and are either perpendicular to the ply plane or inclined by an angle between 0 and approximately 54°. Whether matrix-cracks are critical for the whole laminate depends on the inclination of the crack. Cracks perpendicular to the ply-plane are caused by transverse tensile stresses and/or in-plane shear stresses. Such cracks can be considered tolerable to some extent because the integrity of the laminate is not harmed and the load can be transferred by the fibers. Inclined cracks are caused by pure transverse compressive stresses or a combination of in-plane shear stresses and high transverse compressive stresses. Inclined cracks can be considered harmful for the laminate because they introduce stresses in the thickness direction, which can lead to substantial delamination. The material behaves roughly linear under transverse tensile stresses but shows nonlinear behavior under in-plane shear and transverse compressive stresses. The nonlinear behavior is caused by a stiffness degradation of the material and an accumulation of unrecoverable strains. The stiffness degradation can be explained by the formation of distributed micro-cracks in the matrix material. When the maximum strength is reached, these micro-cracks coalesce into a macroscopically visible crack, which leads to softening material behavior. During unloading of the material, unrecoverable strains can be observed. The unrecoverable strains
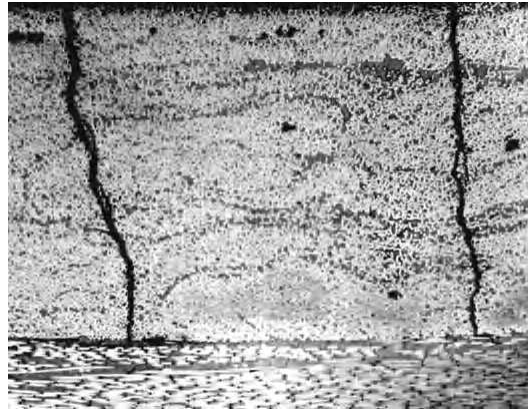
Figure 2.3: Picture of inter-fiber fracture in a UD-reinforced fiber-reinforced poymer laminate [25].

are attributed to unrecoverable openings of micro-cracks and irreversible deformations of the matrix material.

Chapter 3

Constitutive model

In the following, a constitutive model for the prediction of fiber damage, inter-fiber damage, and the accumulation of unrecoverable strains of FRP plies is presented. The constitutive model describes the behavior of the plies, which consist of unidirectional fibers and surrounding matrix material, at a length scale where their properties appear homogeneous. The behavior of the pristine ply, as a member of a laminate, is modeled as linear-elastic and transversely isotropic. To simplify the expressions and their implementation, the entries of second- and fourth-order tensors are given in Voigt-Nye notation [43] (Appendix B). Due to the typically small thickness to width ratios of the plies, the constitutive model is formulated for a shell modeling approach under plane-stress assumptions (Appendix C). After the initial linear behavior, the different failure mechanisms lead to a pronounced nonlinear behavior.

3.1 Internal state variables

The failure mechanisms occurring in FRPs are accompanied by an internal change of the microstructure of the material. These changes take place on a length scale that is smaller than the target resolution of the constitutive model. Consequently, these changes have to be captured by the constitutive equations. Using the theory of thermodynamics with internal variables, the internal change is represented in terms of internal state variables. Thereby the material state is completely defined by a set of state variables at every point in time. With these assumptions, the constitutive equations can be formulated as an

exact differential equation that can be solved in the form of a potential function.

Helmholtz free energy. In the present work, the Helmholtz free energy is used as a potential function for the derivation of the constitutive equations. The Helmholtz free-energy density,

$$\Psi = \Psi^{\mathrm{e}}(\boldsymbol{\varepsilon}, \boldsymbol{\varepsilon}^{\mathrm{p}}, \mathbf{d}) + \Psi_0^{\mathrm{p}}(\tilde{\mathbf{a}}), \tag{3.1}$$

is formulated in terms of the total strain, $\boldsymbol{\varepsilon}$, the plastic strain, $\boldsymbol{\varepsilon}^{\mathrm{p}}$, a vector of effective plastic hardening variables, $\tilde{\mathbf{a}}$, and a vector of damage variables, $\mathbf{d}$. It is assumed that the total Helmholtz free energy can be split into the elastic stored energy Ψ^{E} and the effective plastic energy Ψ_0^{P}. They are independent of each other, which simplifies the implementation and has the advantage that no regularization technique has to be used in the plasticity formulation, because the softening material behavior is entirely treated within the damage formulation.

Damage variables. The damage variables are introduced to model the stiffness degradation caused by fiber fracture and inter-fiber fracture. Following [37, 10], the relation between the damage variables and the compliance tensor is obtained by introducing a fictitious homogeneous material into which spheroidal, oblate voids are successively 'added' to account for the stiffness degradation qualitatively. The volume fraction of the voids is zero for the undamaged material and increases as damage increases. The damage variable d_1 represents damage due to fiber fracture. The corresponding stiffness degradation is obtained by introducing voids into the fictitious material which are perpendicular to the fibers. The damage variables d_2 and d_3 represent damage due to matrix cracking and matrix-fiber debonding. The voids related to d_2 are oriented parallel to the fibers and perpendicular to the ply plane. The voids related to d_3 are oriented parallel to the fibers and one half is rotated by the maximum puck fracture angle [34] in one direction and the second half in the other direction. It is helpful to distinguish between the damage variable d_2 and d_3 because damage due to d_2 is tolerable to some extent, while damage due to d_3 can potentially be critical to the laminate. The compliance tensor of the fictitious material is given by

$$\mathbb{C} = \mathbb{C}^{(0)} \left(\mathbb{I} + \frac{d_1}{1 - d_1} \mathbb{D}^{(1)} + \frac{d_2}{1 - d_2} \mathbb{D}^{(2)} + \frac{d_3}{1 - d_3} \mathbb{D}^{(3)} \right), \tag{3.2}$$

with the fourth-order symmetric identity tensor $\mathbb{I}$, the undamaged compliance tensor $\mathbb{C}^{(0)}$, and the damage contribution tensors

$$\mathbb{D}^{(i)} = \left(\mathbb{I} - \mathbb{S}^{(i)}\right)^{-\mathrm{T}} \ . \tag{3.3}$$

They are obtained through the Mori-Tanaka method as described in [37]. The tensors $\mathbb{S}^{(i)}$ are the Eshelby tensors related to a spheroidal, oblate void of the family (i) inside a transversely isotropic matrix. Since there is no closed-form solution for the Eshelby tensors for transversely isotropic material, they are calculated numerically following [15]. The compliance tensor from equation (3.2) is used because it can be mechanically motivated. According to [24, 23], using an effective field method, like the Mori-Tanaka method, is suitable for homogeneously distributed, parallel crack like voids with very high aspect ratios.

In CDM it is common to introduce effective variables to derive the constitutive equations for the damaged material [31]. The effective variables describe a fictitious undamaged state for which the undamaged constitutive equations can be used. Once the relations between the internal state variables and the effective variables are established, the damaged constitutive equations can be derived from the undamaged ones. The effective stress in CDM is given by

$$\tilde{\boldsymbol{\sigma}} = \mathbb{M} \, \boldsymbol{\sigma} \ , \tag{3.4}$$

where $\mathbb{M}$ is the damage effect tensor and $\boldsymbol{\sigma}$ is the nominal stress. In the present work, the effective elastic strain

$$\tilde{\boldsymbol{\varepsilon}}^{\mathrm{e}} = \boldsymbol{\varepsilon}^{\mathrm{e}} \tag{3.5}$$

is defined according to the principle of elastic strain equivalence. As a result, the relation between the damaged and the undamaged material is given through

$$\mathbb{C} = \mathbb{C}^0 \mathbb{M} \ . \tag{3.6}$$

Together with equation (3.2) this yields the relation for the damage effect tensor

$$\mathbb{M} = \left(\mathbb{I} + \zeta_1 \mathbb{D}^{(1)} + \zeta_2 \mathbb{D}^{(2)} + \zeta_3 \mathbb{D}^{(3)}\right) \ . \tag{3.7}$$

The factors

$$\zeta_i = \frac{d_i}{1 - d_i} \ , \tag{3.8}$$

are called inelastic compliance variables [21]. They can be used interchangeably with the damage variables to describe the compliance of the material. The elastic stored energy of the Helmholtz free energy in equation (3.1) follows as

$$\rho\Psi^{\mathrm{e}}(\boldsymbol{\varepsilon},\boldsymbol{\varepsilon}^{\mathrm{p}},\mathbf{d}) = \frac{1}{2}\left(\boldsymbol{\varepsilon}-\boldsymbol{\varepsilon}^{\mathrm{p}}\right)\cdot\mathbb{M}(\mathbf{d})^{-1}\,\mathbb{E}^0\left(\boldsymbol{\varepsilon}-\boldsymbol{\varepsilon}^{\mathrm{p}}\right)\ , \tag{3.9}$$

with the undamaged elasticity tensor $\mathbb{E}^0$ and the vector of damage variables

$$\mathbf{d} = \begin{pmatrix} d_1 & d_2 & d_3 \end{pmatrix}^{\mathrm{T}}. \tag{3.10}$$

Plastic strain. The plastic strain tensor is introduced to model the unrecoverable strains. In the present work, an additive split of the total strain

$$\boldsymbol{\varepsilon} = \boldsymbol{\varepsilon}^{\mathrm{e}} + \boldsymbol{\varepsilon}^{\mathrm{p}} \tag{3.11}$$

into the elastic strain $\boldsymbol{\varepsilon}^{\mathrm{e}}$ and the plastic strain $\boldsymbol{\varepsilon}^{\mathrm{p}}$ is assumed. Since the plastic strain enters only through the elastic strain into the elastic stored energy Ψ^{E}, its nominal and not its effective variable is used as the internal state variable. Nonetheless, the effective plastic strain is defined through the principle of equivalent plastic strain as

$$\tilde{\boldsymbol{\varepsilon}}^{\mathrm{p}} = \boldsymbol{\varepsilon}^{\mathrm{p}}. \tag{3.12}$$

Internal hardening variables. The internal hardening variables are introduced to describe the strain hardening. The vector of hardening variables $\tilde{\mathbf{a}} = \begin{pmatrix} \tilde{a}_1 & \tilde{a}_2 \end{pmatrix}^{T}$ contains two variables associated with transverse compressive and in-plane shear behavior. The variable $\tilde{a}_1$ can be considered as an effective accumulative plastic transverse compressive strain and the variable $\tilde{a}_2$ can be considered as an effective accumulative plastic in-plane shear angle. The variable $\tilde{a}_1$ is set up to be only positive whereas $\tilde{a}_2$ can be positive or negative. The free energy that is related to the hardening behavior is defined in terms of effective variables as

$$\begin{aligned} \rho\Psi_0^{\mathrm{p}}(\tilde{\mathbf{a}}) =& \frac{\left(\tilde{Y}_3^{\mathrm{c}} - \tilde{Y}_0^{\mathrm{c}}\right)}{1 - e^{-\tilde{a}_1^3 c_1^{\mathrm{p}}}}\tilde{a}_1 + \frac{\left(\tilde{Y}_3^{\mathrm{c}} - \tilde{Y}_0^{\mathrm{c}}\right)}{c_1^{\mathrm{p}}\left(1 - e^{-\tilde{a}_1^3 c_1^{\mathrm{p}}}\right)}e^{-c_1^{\mathrm{p}}\tilde{a}_1} + \\ & \frac{\left(\tilde{S}_3 - \tilde{S}_0\right)}{1 - e^{-\tilde{a}_2^3 c_2^{\mathrm{p}}}}|\tilde{a}_2| + \frac{\left(\tilde{S}_3 - \tilde{S}_0\right)}{c_2^{\mathrm{p}}\left(1 - e^{-\tilde{a}_2^3 c_2^{\mathrm{p}}}\right)}e^{-c_2^{\mathrm{p}}|\tilde{a}_2|}. \end{aligned} \tag{3.13}$$

It is set up such that the compressive and shear behavior are independent of each other and the potential can be split into an compressive and a shear part. The values $\tilde{Y}_0^{\mathrm{c}}$, $\tilde{Y}_3^{\mathrm{c}}$, $\tilde{S}_0$, $\tilde{S}_3$, $\tilde{a}_1^3$, $\tilde{a}_2^3$, c_1^{p}, c_2^{p} are material parameters, that can be obtained from experimental data, which is explained later.

3.2 Dissipation

The evolution laws of the state variables have to fulfill the thermodynamic balance laws. With the Helmholtz free energy from equation (3.1) and the fundamental inequality, the dissipation of the material for an isothermal deformation is given by

$$\mathcal{D} = \boldsymbol{\sigma} \cdot \dot{\boldsymbol{\varepsilon}}^{\mathrm{p}} - \rho \frac{\partial \Psi_0^{\mathrm{p}}}{\partial \tilde{\mathbf{a}}} \cdot \dot{\tilde{\mathbf{a}}} - \rho \frac{\partial \Psi^{\mathrm{e}}}{\partial \mathbf{d}} \cdot \dot{\mathbf{d}} \geq 0 \ , \tag{3.14}$$

which must not be negative for arbitrary evolutions of $\dot{\boldsymbol{\varepsilon}}^{\mathrm{p}}, \dot{\tilde{\mathbf{a}}}, \dot{\mathbf{d}}$. To ensure that the dissipation is not negative for arbitrary evolutions, every term in equation (3.14) must not be negative.

Associated thermodynamic forces for damage.   The vector of associated thermodynamic forces for the damage variables is defined as

$$\mathbf{Y} = -\rho \frac{\partial \Psi^{\mathrm{e}}}{\partial \mathbf{d}} \ . \tag{3.15}$$

They can be interpreted as the amount of elastic energy that is released through the change in the corresponding damage variable. The model is set up in a way that the rate of each damage variable and its corresponding associated thermodynamic force are never negative, individually. The components

$$Y_i = \frac{1}{2(1-d_i)^2} \left(\boldsymbol{\varepsilon} - \boldsymbol{\varepsilon}^{\mathrm{p}} \right) \cdot \mathbb{M}(\mathbf{d})^{-1} \, \mathbb{D}^{(i)} \, \mathbb{M}(\mathbf{d})^{-1} \, \mathbb{E}^0 \left(\boldsymbol{\varepsilon} - \boldsymbol{\varepsilon}^{\mathrm{p}} \right) \tag{3.16}$$

follow from equation (3.9). If the damage variables are between 0 and 1 and the tensors $\mathbb{M}, \mathbb{D}^{(i)}, \mathbb{E}^0$ are positive definite, then $Y_i \geq 0$ for $i = 1, 2, 3$.

Associated thermodynamic forces for plasticity.   For generalized standard materials the associated thermodynamic forces drive the evolution process of the state variables. The thermodynamic driving force for the plastic strain is the stress tensor

$$\boldsymbol{\sigma} = \rho \frac{\partial \Psi^{\mathrm{e}}}{\partial \boldsymbol{\varepsilon}^{\mathrm{p}}} \ . \tag{3.17}$$

In the present work, the driving force for the internal hardening parameters

$$\tilde{\mathbf{A}} = - \left(-\rho \frac{\partial \Psi_0^P}{\partial \tilde{\mathbf{a}}} \right) \tag{3.18}$$
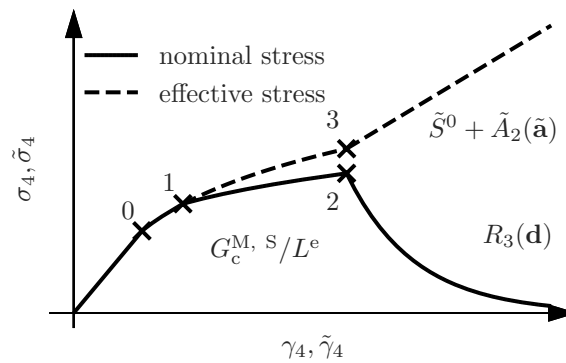
Figure 3.1: The evolution of the nominal shear strength R_3 and the plastic associated thermodynamic force $\tilde{A}_2$ under pure shear loading.

is defined as the negative actual driving force for interpretation purposes. It can therefore be interpreted as the amount of effective stress that is sustainable beyond the initial effective strength. This can be illustrated for instance for the shear strength

$$\tilde{S} = \tilde{S}_0 + \tilde{A}_2(\tilde{a}_2), \tag{3.19}$$

with $\tilde{S}_0$ being the initial shear strength. This definition leads to the expressions

$$\mathbf{\tilde{A}} = \begin{pmatrix} \frac{\tilde{Y}_3^c - \tilde{Y}_0^c}{1 - e^{-\tilde{a}_1^{(3)} c_1^p}} \left(1 - e^{-c_1^p \tilde{a}_1}\right) \\ \mathrm{sign}\,(\tilde{a}_2) \frac{\tilde{S}_3 - \tilde{S}_0}{1 - e^{-\tilde{a}_2^{(3)} c_2^p}} \left(1 - e^{-c_2^p |\tilde{a}_2|}\right) \end{pmatrix}. \tag{3.20}$$

The first component $\tilde{A}_1$ from equation (3.20) is setup in a way that it is always positive and that the strength $Y^c(\tilde{a}_1)$ has the value Y_0^c at $\tilde{a}_1 = 0$ and the value Y_3^c at $\tilde{a}_1 = \tilde{a}_1^{(3)}$. The second component $\tilde{A}_2$ is setup to yield the same behavior as $\tilde{A}_1$ under monotonic loading, but in order to enable kinematic hardening, it changes its sign according to $\tilde{a}_2$. In this way it allows for a declining or even inverse thermodynamic driving force. The evolution of the thermodynamic force $\tilde{A}_2$ from equation (3.20) for a pure shear loading is depicted in Figure 3.1. Its shape is defined by the effective initial yield strength $\tilde{S}_0$, the effective stress $\tilde{S}_3$ at the point 3 with the effective plastic shear angle $\tilde{a}_2^{(3)}$ and the exponent c_2^p that can be chosen to fit experimental data.

3.3 Loading-threshold functions for inter-fiber failure

In the present work, the damage evolution of the damage variables corresponding to inter-fiber fracture is formulated through a constraint problem. To use a strength-based damage condition, the dependence of the damage condition on the internal state variables is required. In the present work, the dependence is given through loading-threshold functions that are defined directly in terms of the damage variables.

Formulating the loading-threshold functions directly in terms of the damage variables entails several challenges. One issue with strength-based loading-threshold functions is, that they cannot be described as injective functions in terms of the damage variables for both hardening and softening. This can lead to problems for the solution procedure at the transition from hardening to softening. To improve the convergence of the solution procedure, effective strength-based driving forces are used instead of nominal strength ones. Effective strengths can be formulated as monotonically increasing functions for both hardening and softening. The effective strengths $\tilde{R}_i$ for $i = (1, 2, 3)$ are defined as effective transverse tensile, effective transverse compressive, and effective in-plane shear strengths. These are the only strengths considered due to the plane stress assumption. The effective strengths

$$\tilde{R}_1 = \mathbb{M}_{22}(\boldsymbol{\zeta}) \ R_1 \tag{3.21}$$

$$\tilde{R}_2 = \mathbb{M}_{22}(\boldsymbol{\zeta}) \ R_2 \tag{3.22}$$

$$\tilde{R}_3 = \mathbb{M}_{44}(\boldsymbol{\zeta}) \ R_3 \tag{3.23}$$

are expressed in terms of the nominal strengths R_i according to equation (3.4) for the effective stress. However, only the corresponding diagonal components are used, because the nominal strengths are obtained from load cases that lead to only one non-zero stress component. Additionally, for each load case, it is assumed that only one inelastic compliance variable is active, whereas the other one is equal to zero. For transverse tension and in-plane shear only $\zeta_2 \neq 0$ and for transverse compression only $\zeta_3 \neq 0$. An exemplary evolution of the nominal in-plane shear strength R_3 is depicted in Figure 3.1 for pure shear loading.

Loading-threshold functions for hardening. In the hardening regime of the material, the nominal strength is an increasing function with damage. According to equations (3.23) and (3.7), the relation between the effective and the nominal strength is linear in $\boldsymbol{\zeta}$. Consequently, the nominal strength is an increasing function as long as the effective strength grows at least linearly in $\boldsymbol{\zeta}$. In the present work, the relations

$$\tilde{R}_1 = \tilde{Y}_1^{\mathrm{T}} + \left(\tilde{Y}_3^{\mathrm{T}} - \tilde{Y}_1^{\mathrm{T}}\right) \frac{\mathbb{M}_{22}\left(\boldsymbol{\zeta}\right) - 1}{\mathbb{M}_{22}\left(\zeta_2^{\mathrm{T,\ c}}\right) - 1} \tag{3.24}$$

$$\tilde{R}_2 = \tilde{Y}_1^{\mathrm{C}} + \left(\tilde{Y}_3^{\mathrm{C}} - \tilde{Y}_1^{\mathrm{C}}\right) \frac{\mathbb{M}_{22}\left(\boldsymbol{\zeta}\right) - 1}{\mathbb{M}_{22}\left(\zeta_3^{\mathrm{C,\ c}}\right) - 1} \tag{3.25}$$

$$\tilde{R}_3 = \tilde{S}_1 + \left(\tilde{S}_3 - \tilde{S}_1\right) \frac{\mathbb{M}_{44}\left(\boldsymbol{\zeta}\right) - 1}{\mathbb{M}_{44}\left(\zeta_2^{\mathrm{S,\ c}}\right) - 1} \tag{3.26}$$

are used for the effective strengths of the material in the hardening regime. The material is considered to be in the hardening regime if the conditions

$$\zeta_1 \frac{\mathbb{C}_{2i}^0 \mathbb{D}_{i2}^{(1)}}{\mathbb{C}_{2j}^0 \mathbb{D}_{j2}^{(2)}} + \zeta_2 + \zeta_3 \frac{\mathbb{C}_{2k}^0 \mathbb{D}_{k2}^{(3)}}{\mathbb{C}_{2l}^0 \mathbb{D}_{l2}^{(2)}} \le \zeta_2^{\mathrm{T,\ c}} \tag{3.27}$$

$$\zeta_1 \frac{\mathbb{C}_{2i}^0 \mathbb{D}_{i2}^{(1)}}{\mathbb{C}_{2j}^0 \mathbb{D}_{j2}^{(3)}} + \zeta_2 \frac{\mathbb{C}_{2k}^0 \mathbb{D}_{k2}^{(2)}}{\mathbb{C}_{2l}^0 \mathbb{D}_{l2}^{(3)}} + \zeta_3 \le \zeta_3^{\mathrm{C,\ c}} \tag{3.28}$$

$$\zeta_1 \frac{\mathbb{C}_{4i}^0 \mathbb{D}_{i4}^{(1)}}{\mathbb{C}_{4j}^0 \mathbb{D}_{j4}^{(2)}} + \zeta_2 + \zeta_3 \frac{\mathbb{C}_{4k}^0 \mathbb{D}_{k4}^{(3)}}{\mathbb{C}_{4l}^0 \mathbb{D}_{l4}^{(2)}} \le \zeta_2^{\mathrm{S,\ c}} \tag{3.29}$$

are satisfied The parameters $\zeta_2^{\mathrm{T,\ c}}, \zeta_3^{\mathrm{C,\ c}}, \zeta_2^{\mathrm{S,\ c}}$ denote the critical inelastic compliance variables at the point of softening onset.

Loading-threshold functions for softening. The challenge for the softening regime is to find an increasing function for the effective strength that at the same time leads to a decreasing nominal strength. Thus, the function for the effective strength must be

sub-linear in $\boldsymbol{\zeta}$. The effective strengths

$$\tilde{R}_1 = \frac{eY_2^{\mathrm{T}}\mathbb{M}_{22}\left(\boldsymbol{\zeta}\right)\,\ln\left(5e^{\frac{\left(\mathbb{C}_{22}(\boldsymbol{\zeta})-\mathbb{C}_{22}\left(\zeta_2^{\mathrm{T},\ \mathrm{c}}\right)\right)}{\mathbb{C}_{22}\left(\zeta_2^{\mathrm{T},\ \mathrm{c}}\right)+C^{\mathrm{T}}}}+e\right)}{5e^{\frac{\left(\mathbb{C}_{22}(\boldsymbol{\zeta})-\mathbb{C}_{22}\left(\zeta_2^{\mathrm{T},\ \mathrm{c}}\right)\right)}{\mathbb{C}_{22}\left(\zeta_2^{\mathrm{T},\ \mathrm{c}}\right)+C^{\mathrm{T}}}}+e} \tag{3.30}$$

$$\tilde{R}_2 = \frac{eY_2^{\mathrm{C}}\mathbb{M}_{22}\left(\boldsymbol{\zeta}\right)\,\ln\left(5e^{\frac{\left(\mathbb{C}_{22}(\boldsymbol{\zeta})-\mathbb{C}_{22}\left(\zeta_3^{\mathrm{C},\ \mathrm{c}}\right)\right)}{\mathbb{C}_{22}\left(\zeta_3^{\mathrm{C},\ \mathrm{c}}\right)+C^{\mathrm{C}}}}+e\right)}{5e^{\frac{\left(\mathbb{C}_{22}(\boldsymbol{\zeta})-\mathbb{C}_{22}\left(\zeta_3^{\mathrm{C},\ \mathrm{c}}\right)\right)}{\mathbb{C}_{22}\left(\zeta_3^{\mathrm{C},\ \mathrm{c}}\right)+C^{\mathrm{C}}}}+e} \tag{3.31}$$

$$\tilde{R}_3 = \frac{eS_2\mathbb{M}_{44}\left(\boldsymbol{\zeta}\right)\,\ln\left(5e^{\frac{\left(\mathbb{C}_{44}(\boldsymbol{\zeta})-\mathbb{C}_{44}\left(\zeta_2^{\mathrm{S},\ \mathrm{c}}\right)\right)}{\mathbb{C}_{44}\left(\zeta_2^{\mathrm{S},\ \mathrm{c}}\right)+C^{\mathrm{S}}}}+e\right)}{5e^{\frac{\left(\mathbb{C}_{44}(\boldsymbol{\zeta})-\mathbb{C}_{44}\left(\zeta_2^{\mathrm{S},\ \mathrm{c}}\right)\right)}{\mathbb{C}_{44}\left(\zeta_2^{\mathrm{S},\ \mathrm{c}}\right)+C^{\mathrm{S}}}}+e} \tag{3.32}$$

are logarithmic in $\boldsymbol{\zeta}$ and lead to decreasing nominal strengths. They are used in the softening regime, when equations (3.27)-(3.29) are not satisfied. The loading-threshold functions for softening are calibrated with nominal ultimate strengths $Y_2^{\mathrm{T}}, Y_2^{\mathrm{C}}, S_2$ and the constants $C^{\mathrm{T}}, C^{\mathrm{C}}, C^{\mathrm{S}}$.

Another challenge lies in calibrating the constants $C^{\mathrm{T}}, C^{\mathrm{C}}, C^{\mathrm{S}}$ according to the dissipated energy in the fracture process. For strain softening continua the solution has to be regularized to obtain mesh-size independent results. In the present work, the crack-band-model [3] is used. For that the loading-threshold functions for the softening branch are scaled by the characteristic element length L^{e}. If nominal strengths are used, the dissipated energy can be prescribed directly. For effective strengths this can only be done indirectly. To apply the crack-band-model, the integral of the nominal stress over the elastic strain from softening onset until total failure has to be prescribed for certain load cases. The integral over the elastic strain can be turned into an integral over the inelastic compliance variables according to

$$
\begin{aligned}
\int_{\boldsymbol{\varepsilon}_{\mathrm{c}}^{\mathrm{e}}}^{\boldsymbol{\varepsilon}_{\infty}^{\mathrm{e}}} \boldsymbol{\sigma} \cdot \mathrm{d}\boldsymbol{\varepsilon}^{\mathrm{e}} &= \int_{\tilde{\boldsymbol{\varepsilon}}_{\mathrm{c}}^{\mathrm{e}}}^{\tilde{\boldsymbol{\varepsilon}}_{\infty}^{\mathrm{e}}} \boldsymbol{\sigma} \cdot \mathrm{d}\tilde{\boldsymbol{\varepsilon}}^{\mathrm{e}} = \int_{\tilde{\boldsymbol{\sigma}}_{\mathrm{c}}}^{\tilde{\boldsymbol{\sigma}}_{\infty}} \boldsymbol{\sigma} \cdot \mathbb{C}^0 \mathrm{d}\tilde{\boldsymbol{\sigma}} \\
&= \int_{\mathbb{M}_{\mathrm{c}}}^{\mathbb{M}_{\infty}} \boldsymbol{\sigma} \otimes \boldsymbol{\sigma} \cdot \mathbb{C}^0 \mathrm{d}\mathbb{M} + \int_{\boldsymbol{\sigma}_{\mathrm{c}}}^{\mathbf{0}} \boldsymbol{\sigma} \cdot \mathbb{C}^0 \mathbb{M} \mathrm{d}\boldsymbol{\sigma} \\
&= \int_{\zeta^{\mathrm{c}}}^{\infty} \left(\boldsymbol{\sigma} \otimes \boldsymbol{\sigma} \cdot \mathbb{C}^0 \frac{\partial \mathbb{M}}{\partial \zeta} + \boldsymbol{\sigma} \cdot \mathbb{C}^0 \mathbb{M} \frac{\partial \boldsymbol{\sigma}}{\partial \zeta} \right) \mathrm{d}\zeta \\
&\overset{!}{=} \mathcal{G}_c / L^{\mathrm{e}} - W \;,
\end{aligned}
\tag{3.33}
$$

using $\mathrm{d}\tilde{\boldsymbol{\sigma}} = \mathrm{d}\mathbb{M}\,\boldsymbol{\sigma} + \mathbb{M}\,\mathrm{d}\boldsymbol{\sigma}$. The values $\boldsymbol{\varepsilon}_{\mathrm{c}}^{\mathrm{e}}$, $\boldsymbol{\sigma}_{\mathrm{c}}$, $\mathbb{M}_{\mathrm{c}}$ and ζ_c denote the entities at the critical point of softening onset and $\boldsymbol{\varepsilon}_{\infty}^{\mathrm{e}}$, $\boldsymbol{\sigma}_{\infty}$ and $\mathbb{M}_{\infty}$ denote the entities at total failure. $\mathcal{G}_{\mathrm{c}}$ is

the total fracture energy density of the whole process and

$$W = \int_0^{\varepsilon_c^e} \boldsymbol{\sigma} \cdot \mathrm{d}\boldsymbol{\varepsilon}^e \tag{3.34}$$

denotes the total energy density from the unloaded state to softening onset without the energy dissipated by plasticity. The operator $\otimes$ denotes the dyadic product of two tensors and $\cdot$ denotes the inner product. The load cases for which the critical fracture energies have to be prescribed correspond to the strengths R_i for in-plane transverse tension, in-plane transverse compression and in-plane shear. Again, it is assumed that only one of the inelastic compliance variables is non-zero. This is the reason why the integral in equation (3.33) can be obtained as the integral over a single inelastic compliance variable. For the aforementioned load cases, the stress tensor is composed of only one entry, which is equal to the particular strength. All other entries are equal to zero. If the stress has only one non-zero component, only this component has to be considered in the inner products of equation (3.33). With equation (3.23) the nominal strengths can be related to effective strengths and the equations (3.30) - (3.32) can be inserted into the integral. Since the loading-threshold functions only depend on $\boldsymbol{\zeta}$, the integral expression from equation (3.33) can be solved for the constants

$$C^{\mathrm{T}} = \frac{2 \left(\mathcal{G}_c^{\mathrm{M,\ T}}/L^e - W^{\mathrm{T}} \right)}{Y_2^{\mathrm{T}2}} \ , \tag{3.35}$$

$$C^{\mathrm{C}} = \frac{2 \left(\mathcal{G}_c^{\mathrm{M,\ C}}/L^e - W^{\mathrm{C}} \right)}{Y_2^{\mathrm{C}2}} \ , \tag{3.36}$$

$$C^{\mathrm{S}} = \frac{2 \left(\mathcal{G}_c^{\mathrm{M,\ S}}/L^e - W^{\mathrm{S}} \right)}{S_2^2} \ . \tag{3.37}$$

The variables $W^{\mathrm{T}}, W^{\mathrm{C}}, W^{\mathrm{S}}$ are obtained by evaluating equation (3.34) for in-plane transverse tension, in-plane transverse compression and in-plane shear, respectively.

3.4 Dissipation potentials

The dissipation potentials are introduced to indicate states in which the internal state variables evolve. The dissipation potentials in this work serve different functions for fiber damage, inter-fiber damage, and plasticity. For fiber damage the dissipation potentials indicate damage initiation. The subsequent evolution of damage is controlled by an explicit damage evolution law. For inter-fiber damage the dissipation potential evolves according to the loading-threshold functions and for plasticity according to the associated thermo-dynamic forces. The evolution of inter-fiber damage and plasticity has to be calculated implicitly such that the dissipation potentials are satisfied.

Fiber damage condition. The fiber damage condition indicates the initiation of fiber damage. The damage evolution is initiated once this condition is fulfilled. The magnitude of the damage is determined by the damage evolution law, which is introduced later. The damage condition for fiber-failure is given by

$$F_{\mathrm{d}}^{\mathrm{F}}(\boldsymbol{\varepsilon}^{\mathrm{e}}) = E_1 \varepsilon_1^{\mathrm{e}} - X^{\mathrm{T}} \tag{3.38}$$

for $\varepsilon_1^{\mathrm{e}} \geq 0$ and by

$$F_{\mathrm{d}}^{\mathrm{F}}(\boldsymbol{\varepsilon}^{\mathrm{e}}) = -E_1 \varepsilon_1^{\mathrm{e}} - X^{\mathrm{C}} \tag{3.39}$$

for $\varepsilon_1^{\mathrm{e}} < 0$. The damage initiation is calibrated by the longitudinal Young's modulus E_1, the transverse Young's modulus E_2, the longitudinal tensile strength X^{T}, and the longitudinal compressive strength X^{C}. The damage initiation is based on the elastic strain tensor because the evolution law is formulated in terms of elastic strains.

Inter-fiber damage condition. The damage condition for inter-fiber-failure is one main part of the constraint problem that is used for the implicit damage evolution. It can be regarded as an auxiliary condition that has to be satisfied throughout the damage evolution. The damage evolution is calculated implicitly so that the damage condition and the evolution equations are satisfied. In the present work, the damage condition for inter-fiber-failure is formulated in terms of effective strengths because it is more suited for ductile behavior than energy based damage conditions. It therefore uses the effective stress and the loading-threshold function from equations (3.24) - (3.32). The damage

condition $F_{\mathrm{d}}^{\mathrm{M}}$ is formulated according to the Puck fracture criterion under plane stress assumption. It is defined as

$$F_{\mathrm{d}}^{\mathrm{M}}(\tilde{\boldsymbol{\sigma}}, \tilde{\mathbf{R}}) = p^{\mathrm{T}}\tilde{\sigma}_2 + \sqrt{\tilde{\sigma}_2^2 \left(\frac{\tilde{R}_3}{\tilde{R}_1} - p^{\mathrm{T}}\right)^2 + \tilde{\sigma}_4^2} - \tilde{R}_3, \qquad (3.40)$$

for $\tilde{\sigma}_2 \geq 0$, as

$$F_{\mathrm{d}}^{\mathrm{M}}(\tilde{\boldsymbol{\sigma}}, \tilde{\mathbf{R}}) = p^{\mathrm{C}}\tilde{\sigma}_2 + \sqrt{(p^{\mathrm{C}}\tilde{\sigma}_2)^2 + \tilde{\sigma}_4^2} - \tilde{R}_3 \qquad (3.41)$$

for $\tilde{\sigma}_2 < 0$ and $\left|\frac{\tilde{\sigma}_2}{\tilde{\sigma}_4}\right| \leq \left|\frac{R^{\mathrm{A}}}{\tau^{\mathrm{c}}}\right|$ and as

$$F_{\mathrm{d}}^{\mathrm{M}}(\tilde{\boldsymbol{\sigma}}, \tilde{\mathbf{R}}) = \frac{\tilde{\sigma}_4^2}{\left(\tilde{R}_3 + \sqrt{\tilde{R}_3 + 2p^{\mathrm{C}}\tilde{R}_2}\right)^2} + \frac{\tilde{\sigma}_2}{\tilde{R}_2} + \frac{\tilde{\sigma}_2^2}{\tilde{R}_2^{\;2}} \qquad (3.42)$$

for $\tilde{\sigma}_2 < 0$ and $\left|\frac{\tilde{\sigma}_2}{\tilde{\sigma}_4}\right| > \left|\frac{R^{\mathrm{A}}}{\tau^{\mathrm{c}}}\right|$. R^{A} is the resistance of the action plane that the loading is acting on, p^{T} and p^{C} are the Puck slope parameters for tension and compression, and τ^{c} is the critical shear stress for Mode C fracture as defined in [34]. Technically, the nominal stress state is plane and according to equation (3.4) the effective stress state does not have to be plane. However, the influence only gets significant for very large ζ_i, where the material can be considered almost failed. This error is accepted in the present work and the Puck criterion for a plane state is used for the effective stresses. The corresponding damage surface

$$\partial F_{\mathrm{d}}^{\mathrm{M}} = \left\{(\tilde{\boldsymbol{\sigma}}, \tilde{\mathbf{R}}) \mid F_{\mathrm{d}}^{\mathrm{M}}(\tilde{\boldsymbol{\sigma}}, \tilde{\mathbf{R}}) = 0\right\} \qquad (3.43)$$

is depicted in stress space in Figure 3.2. It changes its shape and size according to the loading-threshold functions.

Yield condition. The yield condition F_{p} indicates the evolution in $\boldsymbol{\varepsilon}^{\mathrm{p}}$ and $\tilde{\mathbf{a}}$. It is defined as

$$F_{\mathrm{p}}(\tilde{\boldsymbol{\sigma}}, \tilde{\mathbf{A}}) = \frac{\left(\tilde{\sigma}_4 - \alpha\tilde{A}_2\right)^2}{\left(\tilde{S}_0 + (1 - \alpha)\tilde{A}_2\right)^2} + \frac{\tilde{\sigma}_2^2}{\left(Y_0^{\mathrm{C}} + \tilde{A}_1^2\right)} - 1 \; , \qquad (3.44)$$

based on the following assumptions. The first assumption is that the stiff fibers limit the strain ε_1 and hence prevent plastic yielding in fiber direction. In the framework of quasi standard materials this necessitates that the outward normal of the yield surface

$$\partial F_{\mathrm{p}} = \left\{(\tilde{\boldsymbol{\sigma}}, \tilde{\mathbf{A}}) \mid F_{\mathrm{p}}(\tilde{\boldsymbol{\sigma}}, \tilde{\mathbf{A}}) = 0\right\} \qquad (3.45)$$
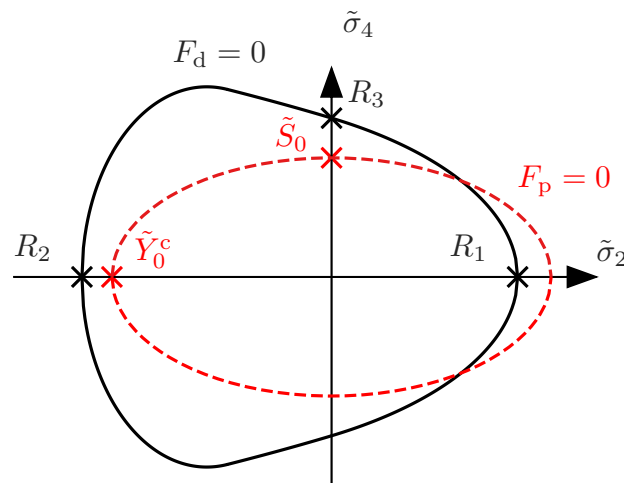
Figure 3.2: Damage and yield surface in $\tilde{\sigma}_4, \tilde{\sigma}_2$-space.

must not have a component in σ_1 direction. The second assumption is that there should be no plastic yielding under pure transverse tensile stresses. This is facilitated by the ellipsoidal yield surface, because the initial transverse compressive yield strength $\tilde{Y}_0^c$ is larger than the transverse tensile strength R_1 for the materials under consideration. In order to enable isotropic as well as kinematic hardening behavior, the yield surface can expand outwards as well as shift its center. Due to the fact that plastic yielding does not occur under transverse tensile stresses, the kinematic hardening effect cannot be provoked under transverse normal stresses. The model is therefore set up that the center of the yield surface is only shifted along the σ_4 axis. The partition into either expanding or shifting is controlled by the parameter α. The parameter α is defined between 0 and 1 and stays constant throughout the analysis. Setting $\alpha = 0$ allows only expanding, i.e. isotropic hardening, whereas setting $\alpha = 1$ only shifting, i.e. kinematic hardening.

3.5 Evolution equations

The evolution equations are used to calculate the internal state variables during the evolution process. In the present work, two different kinds of evolution equations are used. For the fiber damage variable, an explicit evolution law is used. The evolution laws for the inter-fiber damage, the plastic strain, and the hardening variables are given in rate form. Their actual values are obtained through the time-integration of the rate equations. It is critical for the time-integration scheme, that the obtained states satisfy the dissipation potentials.

Evolution of fiber damage. The evolution of the fiber damage variable is defined explicitly because of the simple and efficient implementation of explicit damage evolution laws. Additionally, the benefits of implicit evolution laws do not apply to fiber damage. Fiber-failure is only caused by stresses in fiber direction and hence only one experimental curve is needed for its calibration.

To assure thermodynamic consistency the damage variable has to be a monotonically increasing function over time. This is assured by first calculating a provisional inelastic compliance variable

$$
\begin{aligned}
\zeta_1^\tau = & \frac{1}{\mathbb{C}_{1i}^0 \mathbb{D}_{i1}^{(1)} E_1} \left(\langle \varepsilon_1 \rangle \, \frac{E_1}{X^\mathrm{T}} \exp\left(\frac{X^\mathrm{T} L^\mathrm{e}(E_1 \varepsilon_1 - X^\mathrm{T})}{E_1 \mathcal{G}^{\mathrm{F,\,T}}} \right) \right. \\
& \left. + \langle -\varepsilon_1 \rangle \, \frac{E_1}{X^\mathrm{C}} \exp\left(\frac{X^\mathrm{C} L^\mathrm{e}(E_1 \varepsilon_1 - X^\mathrm{C})}{E_1 \mathcal{G}^{\mathrm{F,\,C}}} \right) - 1 \right) \,,
\end{aligned}
\tag{3.46}
$$

where $\langle \cdot \rangle$ is the Macauley-operator, X^T the fiber tensile strength, X^C the fiber compressive strength, $\mathcal{G}^{\mathrm{F,\,T}}$ the critical energy release rate for longitudinal tension, $\mathcal{G}^{\mathrm{F,\,C}}$ the critical energy release rate for longitudinal compression, and L^e the characteristic element length. The actual damage variable

$$
d_1 = \max_{\tau=(0,t)} \left(\frac{\zeta_1^\tau}{1 + \zeta_1^\tau} \right)
\tag{3.47}
$$

is defined in terms of the maximum provisional inelastic compliance variable over the whole deformation history. The evolution of the provisional damage variable in equation (3.46) is composed of one part for tension and one part for compression. The Macauley operator ensures that only one of both parts is active at a given instance. Each part consists of an

exponential softening law formulated in terms of elastic strains. The softening laws are set up with different parameters for tension and compression.

Evolution of inter-fiber damage. To distinguish fiber and inter-fiber damage, it is helpful to introduce the vector of inter-fiber damage variables

$$\mathbf{d}^{\mathrm{m}} = \begin{pmatrix} \dot{d}_2 \\ \dot{d}_3 \end{pmatrix} . \tag{3.48}$$

Its evolution is given by the rate equation

$$\mathbf{d}^{\mathrm{m}} = \lambda_{\mathrm{d}} \mathbf{D} . \tag{3.49}$$

The damage multiplier λ_{d} represents the magnitude of the change in the inter-fiber damage variables and the vector $\mathbf{D}$ represents the direction or proportion of the damage variables. The damage multiplier λ_{d} is introduced because the damage evolution for inter-fiber damage has to satisfy an additional equation in form of the inter-fiber damage condition and an additional unknown has to be introduced into the system.

If the implicit damage evolution is defined by maximizing the dissipated energy with the constraint of the damage condition, the vector $\mathbf{D}$ is defined as the derivative of the damage condition with respect to $\mathbf{Y}$. In the present work, the inter-fiber damage condition doesn't depend on $\mathbf{Y}$ and the "direction" vector $\mathbf{D}$ has to be derived differently. The fact that the damage variables d_2 and d_3 represent different types of damage, shall be used to derive the damage direction. As in [37], the damage variables d_2 and d_3 represent differently inclined voids in the material. It is assumed that the inclination θ of micro-cracks can be calculated by the Puck fracture criterion by replacing the ultimate strengths by current strengths. The inclination can range from 0 to the maximum fracture angle $\theta_{\max}$. As the whole range of fracture angles cannot be represented by the two damage variables d_2 and d_3, the values in between get approximated as a combination of the extreme values. As a result, the "direction" vector is defined as

$$\mathbf{D} = \begin{pmatrix} 1 - \frac{\sin(\theta)}{\sin(\theta_{\max})} \\ \frac{\sin(\theta)}{\sin(\theta_{\max})} \end{pmatrix} . \tag{3.50}$$

If the Puck fracture angle is equal to zero, only d_2 changes, whereas if it is equal to the maximum fracture angle $\theta_{\max}$, only d_3 changes.

Evolution of plastic internal state variables. To decouple the plasticity and the damage formulation, the principle of maximum dissipation is adopted for the evolution of the plastic state variables. Since $\boldsymbol{\sigma}$, the associated thermodynamic force for $\boldsymbol{\varepsilon}^{\mathrm{p}}$, depends on the damage variables, the plastic dissipation depends on the damage variables. In the present work, the plastic evolution is formulated entirely with effective variables in order to decouple plasticity and damage. Therefore, not the actual plastic dissipation is maximized, but the effective plastic dissipation of the fictitious undamaged material. Maximizing the effective plastic dissipation under the constraint of the yield function F_{p} means maximizing the Lagrangian

$$\tilde{\mathcal{D}}_{\mathrm{p}} = \tilde{\boldsymbol{\sigma}} \cdot \dot{\tilde{\boldsymbol{\varepsilon}}}^{\mathrm{p}} - \tilde{\mathbf{A}} \cdot \dot{\tilde{\mathbf{a}}} - \lambda_{\mathrm{p}} F_{\mathrm{p}}(\tilde{\boldsymbol{\sigma}}, \tilde{\mathbf{A}}) \ , \tag{3.51}$$

with the Lagrange-multiplier λ_{p}. The difference between effective plastic dissipation and nominal plastic dissipation is determind by the difference between the effective stress and the nominal stress. It is important to note that with $\mathbb{M}$ being positive definite the effective and the nominal dissipation have the same sign. The actual difference is small for small damage variables. To limit the difference between the effective and nominal dissipation, plastic yielding is restricted to the hardening regime. The maximum of equation (3.51) is found where its gradient with respect to $\tilde{\boldsymbol{\sigma}}, -\tilde{\mathbf{A}}, \lambda_{\mathrm{p}}$ is zero. This leads to the evolution equations

$$\dot{\tilde{\boldsymbol{\varepsilon}}}^{\mathrm{p}} = \lambda_{\mathrm{p}} \frac{\partial F_{\mathrm{p}}(\tilde{\boldsymbol{\sigma}}, \tilde{\mathbf{A}})}{\partial \tilde{\boldsymbol{\sigma}}} \ , \tag{3.52}$$

$$\dot{\tilde{\mathbf{a}}} = \lambda_{\mathrm{p}} \frac{\partial F_{\mathrm{p}}(\tilde{\boldsymbol{\sigma}}, \tilde{\mathbf{A}})}{\partial \left(-\tilde{\mathbf{A}}\right)} = -\lambda_{\mathrm{p}} \frac{\partial F_{\mathrm{p}}(\tilde{\boldsymbol{\sigma}}, \tilde{\mathbf{A}})}{\partial \tilde{\mathbf{A}}} \tag{3.53}$$

for the plastic state variables.

3.6 Viscous regularization

Strain softening continua typically lead to convergence problems of the global Newton solver in Finite Element analyses. Therefore, viscous regularization is introduced to increase the performance of the numerical algorithm. Newton's method requires differentiable functions for fast convergence. This is not the case for the constitutive model at the transition from hardening to softening. To regularize the solution, the vector of viscous damage variables

$$\dot{\mathbf{d}}^{\mathrm{v}} = \frac{1}{\eta}\left(\mathbf{d} - \mathbf{d}^{\mathrm{v}}\right) \tag{3.54}$$

is introduced, with η being the viscosity parameter. The viscous damage variables are then substituted for the damage variables into the expression

$$\boldsymbol{\sigma} = \mathbb{M}^{-1}\left(\mathbf{d}^{\mathrm{v}}\right)\ \tilde{\boldsymbol{\sigma}} \tag{3.55}$$

to obtain the nominal stress.

Chapter 4

Implementation

To use the constitutive model with the Finite Element Solver ABAQUS/Standard 2019 (SIMULIA, Providence, RI, USA), it has to be implemented in a material subroutine UMAT. For that discrete values for the dependent variables, namely the stress and the internal state variables, have to be obtained from the continuous constitutive equations. The constitutive integration algorithm is used to update the dependent variables at the beginning of the increment, denoted with the superscript (n), to obtain the dependent variables at the end of the increment, denoted with the superscript $(n+1)$. The difference between the dependent variables at the beginning and the end of the increment is denoted with a Δ.

4.1 Constitutive integration algorithm

Since there is no closed-form solution that solves the governing constitutive equations while satisfying the dissipation potentials, a numerical integration scheme is used. The integration scheme is composed of an elastic predictor step and a plastic and/or a damage corrector step.

Elastic predictor step. The procedure starts with the strain $\boldsymbol{\varepsilon}^{(n+1)}$ of the current increment and the state variables $\boldsymbol{\varepsilon}^{\mathrm{p}\,(n)}, \tilde{\mathbf{a}}^{(n)}, \mathbf{d}^{\mathrm{v}\,(n)}$ of the previous time increment. In the elastic-predictor step the internal state variables of the material are assumed constant. Under this assumption an effective trial stress $\tilde{\boldsymbol{\sigma}}^{(\mathrm{trial})}$ is calculated.
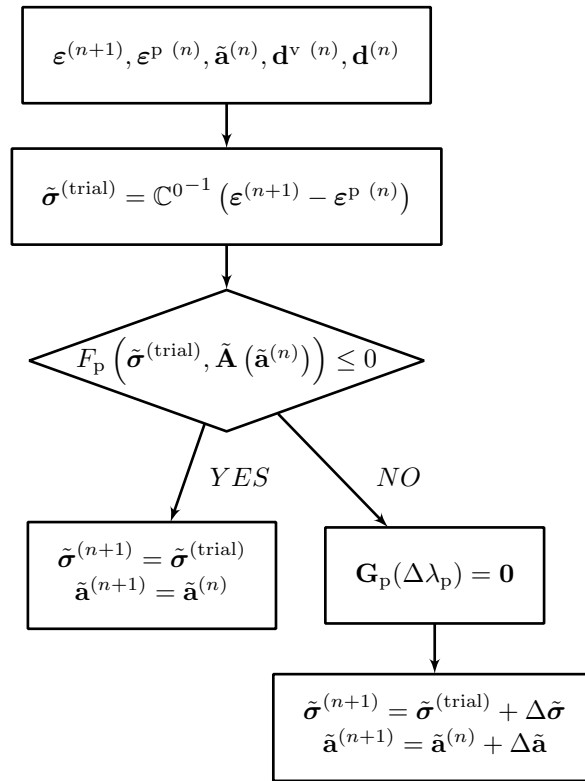
Figure 4.1: Procedure for the plastic-corrector step.

Plastic corrector step. The evolution of the plastic state variables depends only on the effective variables and is independent of the damage variables. This enables to calculate the plastic evolution first and solve the damage evolution afterwards. The procedure for the plastic corrector is illustrated in Figure 4.1. The effective trial stress is used to check if the yield condition F_p indicates plastic yielding. If the yield condition is satisfied, the effective stress for the current increment is set equal to the effective trial stress. If the yield condition is not satisfied, the plastic evolution equations

$$
\mathbf{G}_\mathrm{p}(\Delta\lambda_\mathrm{p}) = \begin{pmatrix} \mathbb{C}^0 \Delta\tilde{\boldsymbol{\sigma}} + \Delta\lambda_\mathrm{p} \frac{\partial F_\mathrm{p}}{\partial \tilde{\boldsymbol{\sigma}}} \\ \Delta\tilde{\mathbf{a}} + \Delta\lambda_\mathrm{p} \frac{\partial F_\mathrm{p}}{\partial \tilde{\mathbf{A}}} \\ F_\mathrm{p}\left(\Delta\tilde{\boldsymbol{\sigma}}, \tilde{\mathbf{A}}\left(\Delta\tilde{\mathbf{a}}\right)\right) \end{pmatrix} = \mathbf{0} \tag{4.1}
$$

have to be solved for the plastic multiplier $\Delta\lambda_\mathrm{p}$. Once $\Delta\lambda_\mathrm{p}$ is known, the other solution variables are updated. At this point the solution for effective variables at the end of the increment are known and the solution only depends on the damage variables.

Damage corrector step. The effective variables at the end of the plastic step are used to infer whether a damage corrector step is needed. The procedure for the damage step is illustrated in Figure 4.2. The fiber damage condition and the evolution law for fiber damage are independent of inter-fiber damage and are therefore solved first. The fiber damage condition F_d^F indicates states in which fiber damage evolves. If the fiber damage condition is satisfied, the damage at the end of the increment is set to the value at the beginning of the increment. If the fiber damage condition is not satisfied, the provisional inelastic compliance variable is calculated according to equation (3.46). Following equation (3.47), the actual fiber damage variable is updated if the resulting damage variable is larger than any previously attained one.

A change of the inter-fiber damage variables is checked by the inter-fiber damage condition F_d^M. If the inter-fiber damage condition is satisfied, the inter-fiber damage variables $\mathbf{d}^m = (d_2 \; d_3)^T$ at the end of the increment are set to the values at the beginning of the increment. If the inter-fiber damage condition is not satisfied, the damage evolution equations

$$\mathbf{G}_d(\Delta\lambda_d) = \begin{pmatrix} \Delta\mathbf{d} - \Delta\lambda_d \mathbf{D}^{(n)} \\ F_d\left(\tilde{\boldsymbol{\sigma}}^{(n+1)}, \tilde{\mathbf{R}}\left(\Delta\mathbf{d}\right)\right) \end{pmatrix} = \mathbf{0} \tag{4.2}$$

are solved for the damage multiplier $\Delta\lambda_d$. The damage multiplier is used to update the inter-fiber damage variables.

To apply the viscous regularization, equation (3.54) has to be integrated numerically. Using an implicit Euler integration scheme, the viscous damage variables at the end of the increment can be obtained through

$$\mathbf{d}^{v\,(n+1)} = \frac{\Delta t\,\mathbf{d}^{(n+1)} + \eta\,\mathbf{d}^{v\,(n)}}{\Delta t + \eta} \; . \tag{4.3}$$

The viscous damage variables are then substituted into equation (3.55) to calculate the nominal stress at the end of the increment.
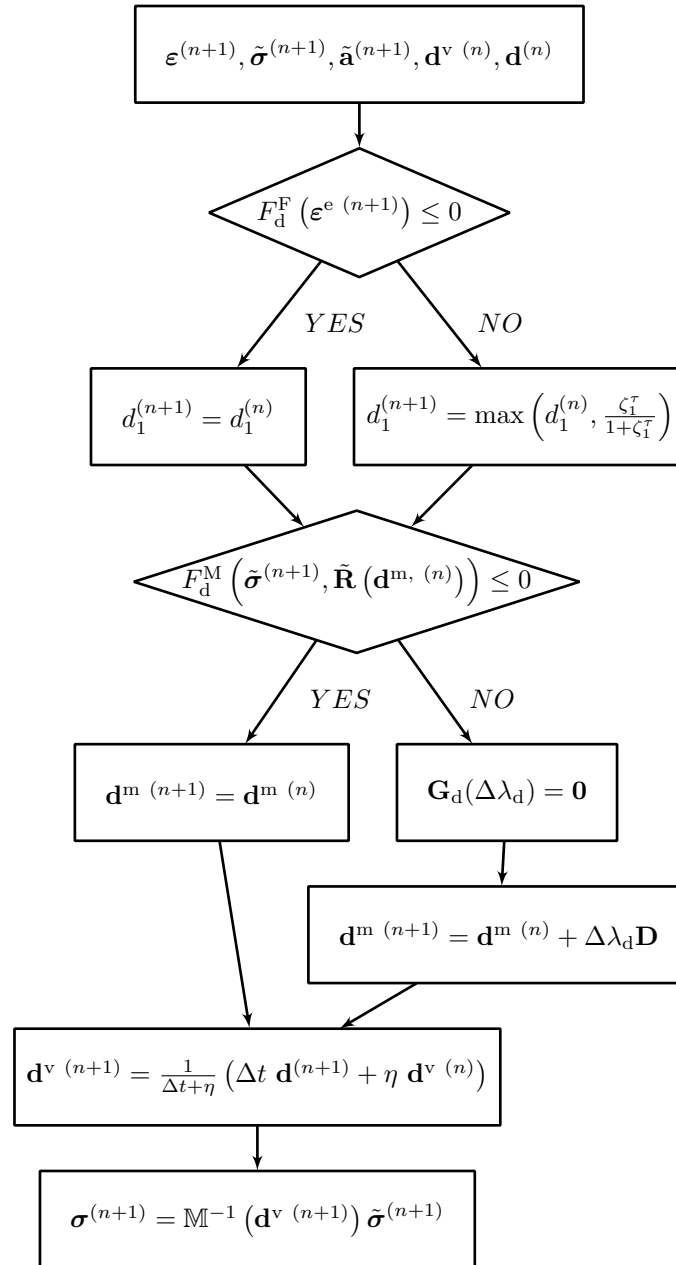
Figure 4.2: Procedure for the damage-corrector step.

4.2   Algorithmic consistent material tangent matrix

The application of the Finite-Element-Method leads to a nonlinear system of equations, which is typically solved by the Newton-Raphson-Method. To ensure fast convergence of the method, the Jacobian of the system of equations is required. The global Jacobian of the system can be assembled from the algorithmic consistent material tangent matrices at every integration point. The algorithmic consistent material tangent matrix for the proposed material model is given by

$$\mathbb{E}^{\mathrm{t}} = \left(\mathrm{L}^{\sigma} - \mathrm{L}^{\sigma,\mathrm{M}}\, \mathrm{L}^{\mathrm{M}\,-1}\, \mathrm{L}^{\mathrm{M},\sigma} - \mathrm{L}^{\sigma,\mathrm{P}}\, \mathrm{L}^{\mathrm{P}\,-1} \left(\mathrm{L}^{\mathrm{P},\sigma} - \mathrm{L}^{\mathrm{P},\mathrm{M}}\, \mathrm{L}^{\mathrm{M}\,-1}\, \mathrm{L}^{\mathrm{M},\sigma} \right) \right)^{-1} \tag{4.4}$$

$$\left(\left(\mathrm{L}^{\sigma,\mathrm{F}} + \left(\mathrm{L}^{\sigma,\mathrm{P}}\, \mathrm{L}^{\mathrm{P}\,-1}\, \mathrm{L}^{\mathrm{P},\mathrm{M}} - \mathrm{L}^{\sigma,\mathrm{M}} \right) \mathrm{L}^{\mathrm{M}\,-1}\, \mathrm{L}^{\mathrm{M},\mathrm{F}} - \mathrm{L}^{\sigma,\mathrm{P}}\, \mathrm{L}^{\mathrm{P}\,-1}\, \mathrm{L}^{\mathrm{P},\mathrm{F}} \right) \mathrm{L}^{\mathrm{F}\,-1}\, \mathrm{L}^{\mathrm{F},\varepsilon} - \mathbb{I} \right) \ . \tag{4.5}$$

The expressions $\mathrm{L}^{\sigma}, \mathrm{L}^{\sigma,\mathrm{P}}, \mathrm{L}^{\sigma,\mathrm{M}}, \mathrm{L}^{\sigma,\mathrm{F}}, \mathrm{L}^{\mathrm{P},\sigma}, \mathrm{L}^{\mathrm{P}}, \mathrm{L}^{\mathrm{P},\mathrm{M}}, \mathrm{L}^{\mathrm{P},\mathrm{F}}, \mathrm{L}^{\mathrm{M},\sigma}, \mathrm{L}^{\mathrm{M}}, \mathrm{L}^{\mathrm{M},\mathrm{F}}, \mathrm{L}^{\mathrm{F}}, \mathrm{L}^{\mathrm{F},\varepsilon}$ are auxiliary matrices which are given in the Tables A.1-A.3 in Appendix A. Depending on which mechanisms are occurring at a given instance, only certain auxiliary matrices enter into the expression. All auxiliary matrices with P in the superscript only enter in a plastic step, all matrices with a M in the superscript only enter when inter-fiber damage occurs and all matrices with a F in the superscript only enter when fiber damage occurs.

Chapter 5

Applications

To assess the predictive capabilities of the constitutive model, its predictions are computed for three applications. The applications are set up to asses different aspects of the constitutive model. The application in Section 5.1 targets the plasticity formulation, especially the kinematic hardening effect. To have a complete understanding of the response of the material, the prediction is obtained for a single element test with a homogeneous stress and strain field.

To test the predictions for damage and plasticity on a structure, simulations of an open hole tension test with different laminate stackings are performed in Section 5.2. The simulations for the open hole tension test is a special challenge for the damage evolution especially with softening material behavior. It also represents a test for the numerical efficiency and robustness of the constitutive model. To obtain simulation results in a reasonable amount of time, the constitutive model has to obtain the solution for a given strain increment reliably.

To assess the convergence for an even larger structure, the constitutive model is used to model the behavior of the tow material in a fabric laminated structure in Section 5.3. As there is a high number of tows which have to be resolved in the numerical model, they are meshed with a relatively coarse mesh. As a result, the stress field of each tow can not be resolved as accurately as in the open hole tension test. The results shall provide insights on the convergence of the constitutive model for a coarse mesh.
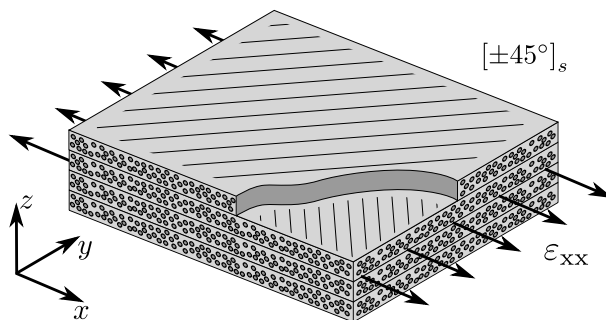
Figure 5.1: The tension load step of a tension compression load cycle applied to a $[\pm45°]_{\mathrm{s}}$-laminate.

5.1 Cyclic loading of a $[\pm45°]_{\mathrm{s}}$-laminate

In the following the predictions of the proposed constitutive model are compared to the experimental data presented in [9]. In the considered experiment a $[\pm45°]_{\mathrm{s}}$-laminate with the material system Cycom977-2-35/40-12KHTS-134-300 with a fiber volume fraction of 60% is loaded in a tension-compression load cycle. The tensile loading of the $[\pm45°]_{\mathrm{s}}$-laminate, depicted in Figure 5.1, leads to a predominant shear deformation in the coordinate systems of every ply. The numerical predictions were obtained with a simulation of one layered shell element.

5.1.1 Calibration of the material parameters

The ply material is made of the prepreg system Cycom977-2-35/40-12KHTS-134-300. To apply the constitutive model, the elastic properties of the ply, the nominal strengths, the fracture energies, the stress-strain curves for transverse (in-plane) compression, and in-plane shear, the input parameters for the Puck failure criterion and the viscous regularization parameters are required. The elastic properties of the ply, given in Appendix E in Table E.1, are taken from [12]. The remaining parameters, given in Appendix E in the Tables E.2 - E.4, are concerned with the nonlinear behavior of the ply. The nominal strengths X^{T}, X^{C}, and Y_2^{T} are taken from [12]. Since the plastic yielding and the hardening damage are negligible under transverse (in-plane) tension, the parameters Y_0^{T}, Y_1^{T}, and $\tilde{Y}_3^{\mathrm{T}}$ are estimated close to Y_2^{T}. The fracture energies $\mathcal{G}^{\mathrm{M,\ T}}$ and $\mathcal{G}^{\mathrm{M,\ S}}$ are taken from [20], where they are used for the material system IM7/8552. The fracture energies
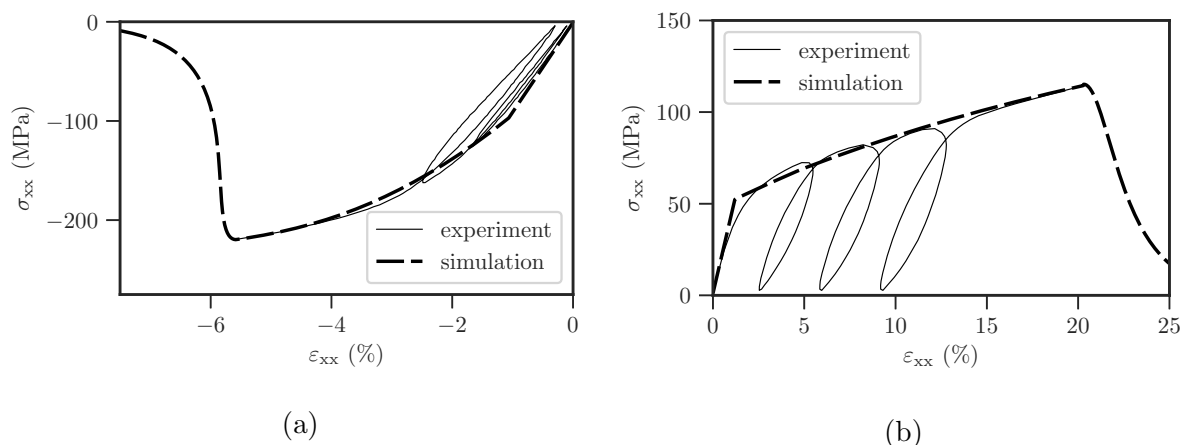
Figure 5.2: The stress-strain curve of the experiment and the simulation of an uniaxial compression test of a $[(90)_{32}]$-laminate (a) with the material system Cycom977-2-35/40-12KHTS-134-300, and the stress-strain curve of the experiment and the simulation of an uniaxial tension test of a $[(+45/-45)_8]_{\mathrm{s}}$-laminate (b).

$\mathcal{G}^{\mathrm{F,\,T}}$, $\mathcal{G}^{\mathrm{F,\,C}}$, and $\mathcal{G}^{\mathrm{M,\,C}}$ are taken from [28], where the material system T300/1034-C is considered. The parameters Y_0^{C}, Y_1^{C}, Y_2^{C}, $\tilde{Y}_3^{\mathrm{C}}$, and c_1^{p} are set according to the stress-strain curve for transverse (in-plane) compression depicted in Figure 5.2a, which was obtained by an uniaxial compression test of a $[(90)_{32}]$-laminate. The parameters S_0, S_1, S_2, $\tilde{S}_3$, and c_2^{p} are set according to the stress-strain curve for in-plane shear depicted in Figure 5.2b, which was calculated from a uniaxial tension test of a $[(+45/-45)_8]_{\mathrm{s}}$-laminate. The parameters p^{T} and p^{C} are chosen according to the recommendations in [34]. The viscous regularization parameter η is set to $2\mathrm{E}{-}5\ s$, to be of similar size as the time step when material softening occurs. For the calibration of the kinematic hardening behavior, only the parameter α is needed, which is set to $\alpha = 1$ to enable pure kinematic hardening.

5.1.2   Results

The resulting stress-strain predictions are depicted in Figure 5.3 for the experiment, a simulation with only plasticity and a simulation with plasticity and damage. The applied strain first leads to a linear stress-strain relation in both, the experiment and the simulations. The nonlinearity is first visible in the experiment and initiated at a slightly higher strain in the simulations. After reaching point "1" with a stress of $\sigma_{\mathrm{xx}}^{(1)} = 190$ MPa the
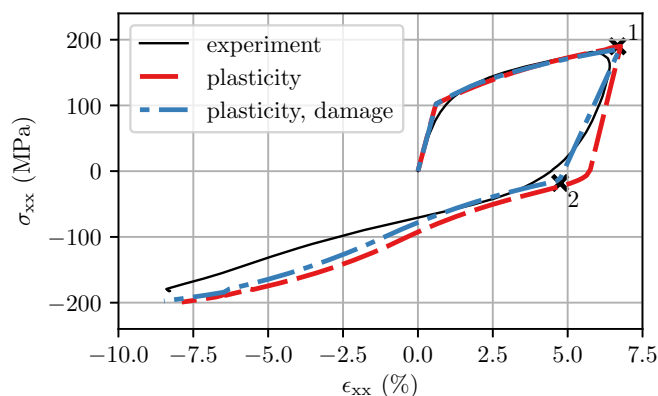
Figure 5.3: Prediction (red, blue) of stress-strain response of a $[\pm 45°]^{s}$-laminate with the material system Cycom977-2-35/40-12KHTS-134-300 under a tension-compression load cycle compared to experiment (black).

specimen first gets unloaded and then loaded in reverse direction. The initial unloading behavior can be considered linear, even though the experiment shows some deviations due to the experimental set up. Both simulations predict different results for the stiffness during unloading, where the result of the simulation with damage lies closer to the experiment. Due to the smooth transition from the linear to nonlinear response, the onset of yielding in the opposite direction cannot be determined precisely for the experiment. The simulation with damage and plasticity starts yielding in the opposite direction at point "2" with a stress of $\sigma_{xx}^{(2)} = -18$ MPa. The fact, that the difference $\Delta\sigma_{xx} = \sigma_{xx}^{(1)} - \sigma_{xx}^{(2)} = 208$ MPa between the stress at point 1 and 2 is approximately twice the stress of initial plastic yielding, suggests pure kinematic hardening.

To further demonstrate the kinematic hardening behavior, the stress path of the simulation with damage and plasticity is depicted in Figure 5.4. The stress path is linear until it intersects the initial yield surface ∂F_{p}^{I}. The following accumulation of plastic strains and the evolution of the internal hardening variables lead to a shift of the yield surface until the load reversal point "1". During this process the yield surface is only shifted and not expanded compared to ∂F_{p}^{I}. After the load reversal, the stress path shows a linear behavior as long as it crosses the yield surface ∂F_{p}^{II}, which stays constant until point "2" is reached. At this point plastic yielding occurs in the opposite direction and the yield surface is shifted in negative σ_{4} direction.
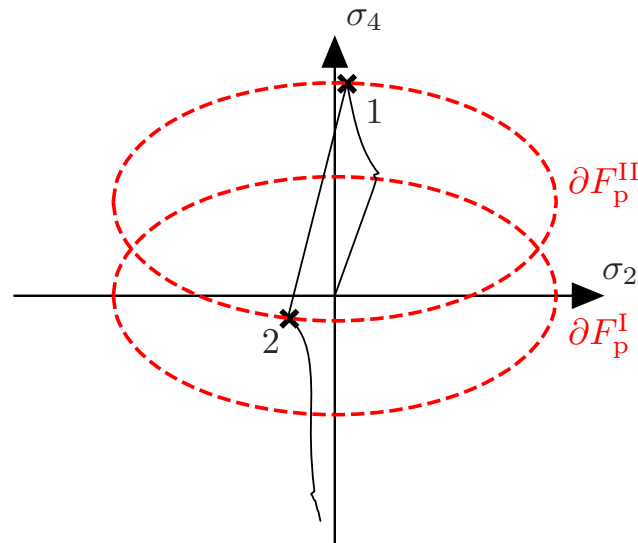
Figure 5.4: Stress path (thin solid line), initial yield surface $\partial F_{\mathrm{p}}^{I}$ and yield surface $\partial F_{\mathrm{p}}^{II}$ at load reversal point in the coordinate system of the bottom ply.

5.1.3 Discussion

The comparison of the simulations with the experimental data shows, that the constitutive model is able to obtain accurate predictions for platic yielding under a shear loading of the ply. The model is set up in an anisotropic manner, to allow for different behaviors under transverse compression and in-plane shear, which can be calibrated independently. The prediction for the stress-strain response for the initial tensile loading lies very close to the experiments. It can be concluded that the evolution of the thermodynamic associated forces for plasticity $\tilde{\mathbf{A}}$ can be calibrated according to the characteristic behavior of the experimental shear stress-shear-angle curve. The results for the reverse loading show that the kinematic hardening effect, that is observed with the Cycom977-2-35/40-12KHTS-134-300 material system, can be reproduced. During unloading, the behavior is better captured by the simulation with damage than by the one without.
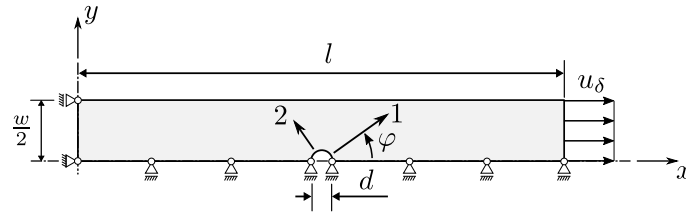
Figure 5.5: Loading and dimensions of the open hole specimen.

5.2   Open hole tension test

To assess the capabilities of the constitutive model, its predictions are computed for the open hole tension tests presented in [12]. The predictions are made for a $[\pm 45]_\mathrm{s}$ and a $[0/90]_\mathrm{s}$-laminate. In the experiments, the specimen is clamped at both ends. To reduce the complexity of the numerical model, only the free length of the specimen is model in the simulations. The specimen and the boundary conditions used for the simulations are depicted in Figure 5.5, with the dimensions $l = 130$ mm, $w = 32.5$ mm, $d = 6.4$ mm, and a thickness of 2 mm. The geometry, the boundary conditions, and the loading are symmetric with respect to the x, y-plane. The ply orientation is not symmetric. Since failure is expected to occur in a distance from the symmetry-plane, its dependence on the boundary conditions at the symmetry plane are assumed to be negligible. To reduce the size of the numerical model, symmetry boundary conditions are used in the $x - z$ plane and the $x - y$ plane and only one half of the width and one half of the thickness of the specimen is modeled.

In the present work, only the intra-ply failure shall be considered and the failure due to delamination is not modeled. Because of the small thickness to width ratio of the specimen, the model is discretized by eight-noded, fully integrated shell elements with layered section definitions and 5 section points. The simulations are performed with a small strain assumption. The same material system as in Section 5.1.1 is used and the material parameters are calibrated in the same way.

5.2.1   Results for the $[\pm 45]_\mathrm{s}$-laminate

Plasticity.   The tensile loading of the $[\pm 45]_\mathrm{s}$ specimen leads to predominant shear deformation of the individual plies. At a load of 6.08 kN, the shear stress leads to the initiation
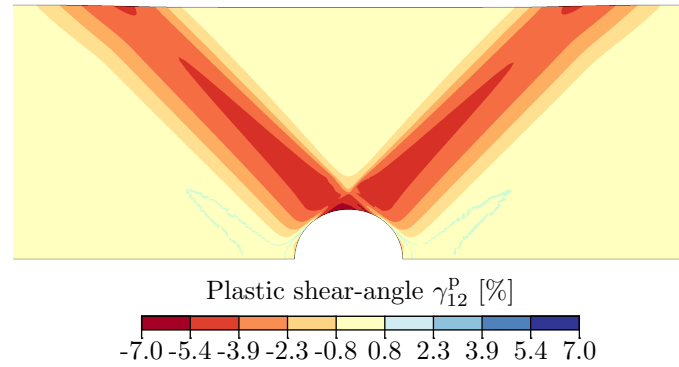
Plastic shear-angle γ_{12}^{p} [%]

-7.0 -5.4 -3.9 -2.3 -0.8 0.8 2.3 3.9 5.4 7.0

Figure 5.6: Plastic shear angle γ_{12}^{p} in the $+45°$ ply of the $[\pm 45]_{\mathrm{s}}$-laminate at a load of 13.98 kN.

of plastic yielding at the edge of the hole at $y = l/2$. During plastic yielding, the material is hardening and large areas of the specimen deform plastically. The plastic deformation of the $+45°$ ply is depicted in Figure 5.6 at a load of 13.98 kN. The regions of high plastic deformation are oriented in a $45°$ angle, parallel to the fibers and their width is roughly equal to the diameter of the hole.

Damage. Initially, the damage occurs in the regions of plastic yielding and is accompanied by hardening behavior. At a load of 13.98 kN the damage localizes at the two points where the fibers, oriented in a $\pm 45°$ angle, cut the hole tangentially. At these points, the damage is caused by a combination of transverse tensile and in-plane shear stresses. The ratio σ_2/σ_4 is influenced by the hole diameter of the specimen and decreases with increasing hole diameter. For the geometry under consideration $\sigma_2/\sigma_4 > Y_3^T/S_3$ and consequently the transverse tensile stress is the main reason for the initiation of damage localization. The region of softening damage develops along the $\pm 45°$ angle in positive y-direction, as depicted in Figure 5.7. At a distance from the hole, the transverse tensile stress is less dominant and the damage is mainly driven by the shear stress.

5.2.2 Results for the $[0/90]_{\mathrm{s}}$-laminate

Plasticity. Due to the stiff fibers, the $0°$ plies transfer most of the load in the $[0/90]_{\mathrm{s}}$-laminate. The hole intersects some fibers of the $0°$ plies which causes a strong stress concentration in the vicinity of the hole. At the edge of the hole, the normal stress in
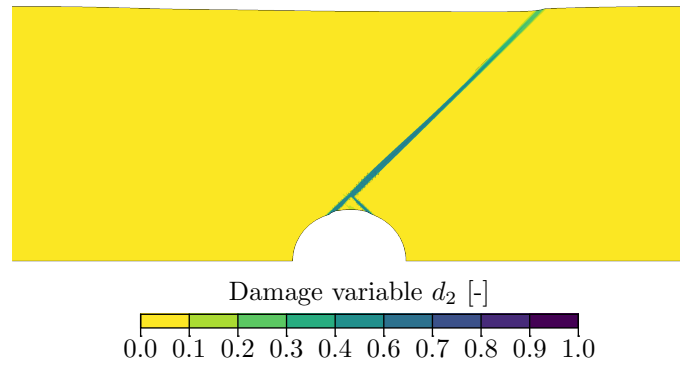
Damage variable d_2 [-]

0.0 0.1 0.2 0.3 0.4 0.6 0.7 0.8 0.9 1.0

Figure 5.7: Damage variable d_2 in the $+45°$ ply of the $[\pm45]_s$-laminate at a load of 13.98 kN.

Plastic shear-angle γ_{12}^{p} [%]

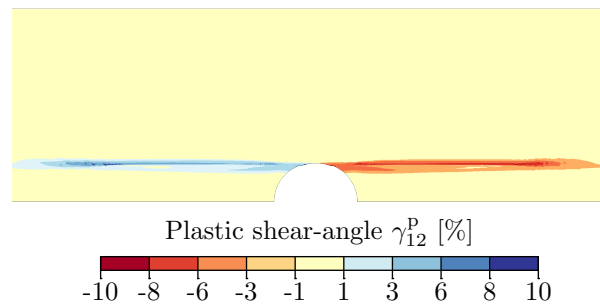-10 -8 -6 -3 -1 1 3 6 8 10

Figure 5.8: Plastic shear angle γ_{12}^{p} in the $0°$ ply of the $[0/90]_s$-laminate at a load of 30.36 kN.

the fibers, that are intercepted by the hole, gets transferred into the continuous fibers through shear stresses. At a comparatively low load of 300 N the resulting shear stress concentration leads to initiation of plastic yielding in the vicinity of the hole. The stress concentration acts very locally and the size of the plastic region is very small. Further increase of the load leads to an expansion of the plastic zone parallel to the loading direction. The plastic shear angle is depicted in Figure 5.8 for a load of 30.36 kN.

Damage. Similar to the plastic yielding, damage gets initiated at a comparably low load of 800 N and only evolves in a small area. Shortly after the damage initiation, it starts to localize. The area of softening damage develops along the fibers in the loading direction as depicted in Figure 5.9. It can be regarded as stable crack growth which decreases the stress concentration at the hole in the 0°-ply. Total failure occurs when the fiber strength in the central cross-section with continuous fibers is reached. At this point,
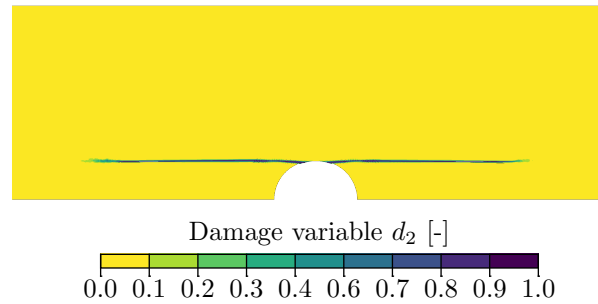
Figure 5.9: Damage variable d_2 in the 0° ply of the $[0/90]_s$-laminate at a load of 30.36 kN.

an instable crack develops perpendicular to the loading direction.

5.2.3 Discussion

The objective of the simulations of the open hole tension test is to check if it is feasible to perform structural computations with the proposed constitutive model. The results show that the phenomena of inter-fiber damage and plastic yielding can be predicted in a structural component. In the case of the $[\pm45]_s$ laminate, the distributed evolution of plastic yielding as well as damage during the hardening regime is modeled. Additionally, the localization of damage into a macroscopic crack, that leads to the total failure of the laminate, can be predicted. It is to note that the model can predict the initiation of damage due to the transverse normal stress as well as the subsequent evolution of the same kind of damage driven by shear stresses. For the $[0/90]_s$ laminate the damage starts to localize very early and the constitutive model is able to predict the stable crack growth in loading direction.

For structural computations the robustness of the solution algorithm is critical. During a simulation of large structures, the material subroutine is called many times with very different loading conditions. Another challenge is that during crack propagation, certain integration points experience strain increments of over 50%. If the constitutive model fails to provide a solution for an increment in a single integration point, the solver will try to find a solution with a smaller increment size. If this situation occurs too often, the increment size will get very small, which leads to very long computation times.

The simulations for the open hole tension test show, that the constitutive model is able to reliably provide solutions for the given strain increments. At this point, certain

design decisions for the constitutive model come into play. The fact that the model is set up in terms of the effective stress, leads to reliable predictions at the transition from hardening to softening damage. This is not the case, when the nominal stress is used. Additionally, using an independent formulation for plasticity and damage leads to the solution of two simple systems of equations as opposed to a complex coupled system.

5.3 Fabric laminated structure

To test the predictive capabilities and the numerical performance of the constitutive model for a complex structure, it is used to model the material behavior of the tow material of a laminated fabric structure. The numerical progressive failure analysis of large structures made of fabric composites, involving nonlinear and softening material behavior, entails several challenges. Firstly, the geometry of the mesostructure of the fabric composite ply has to be resolved to be able to model the failure mechanisms. Traditionally, fabric composites have been modeled using laminate analogy, where the weft and warp yarns are approximated as UD-plies, respectively. This approach, however, does not capture the effects arising from the yarn undulations and the heterogeneous mesostructure. It neglects the resulting high stress concentrations on the mesoscale, which trigger nonlinear effects even under comparably low loading. Consequently, these nonlinear effects cannot be modeled in a homogenized way, which necessitates a detailed model in regions where the nonlinearities are expected.

Because the mesostructure of weaves and braids is complex, typically idealized geometries are used for Finite Element (FE) simulations. Such models have first been developed for continuum elements and then for shell elements [13]. The latter takes advantage of the thin geometry of the tows and thereby reduces the number of degrees of freedom significantly. However, even the shell based ply modeling leads to a high computational effort, which makes it infeasible to resolve the whole mesostructure of large structural components. This can be overcome by an embedding approach [38], where the geometry is only resolved in the region of interest, whereas the rest of the structure is modeled in a homogenized way.

Another challenge is to model the nonlinear tow behavior of the fabric plies. Since the tows are reinforced only in one direction, constitutive models developed for UD-plies can be used, which have extensively been studied. However, most of these constitutive models have been developed for the use of quasi-isotropic laminates. Quasi-isotropic laminates are composed of UD-plies with reinforcement fibers in multiple directions and hence their failure behavior is largely determined by the brittle behavior of the fibers. The mechanism concerning the matrix material, i.e. damage and plasticity, play a minor role and their

ductile behavior is not treated in most constitutive models. Since every ply in a biaxial braid or weave only has two fiber-reinforced directions, matrix damage and plasticity play an increased role. Therefore, it is essential to use constitutive models, which are capable of predicting the ductile mechanisms of the tows.

The aim of this application is to combine an efficient modeling approach for an embedded fabric region and a constitutive model for damage and plasticity of the fabric in order to enable the progressive failure analysis of a large scale fabric composite structure. Therefore an embedding approach is used, where the region, in which the nonlinear effects are expected to initiate, is resolved by a shell modeling approach [13]. The nonlinear tow behavior is modeled by the constitutive model developed in this work. The simulations are carried out with the Finite Element Software ABAQUS/Standard 2018 (SIMULIA, Providence, RI, USA) using an implicit time integration scheme.

5.3.1 Modeling

To test the proposed modeling approach for structural components, it is applied to the C-profile beam under four point bending load, depicted in Figure 5.10. The wall of the C-profile consists of a $\pm 30°$ biaxial multilayer braid with two plies in an out-of-phase stacking sequence. The dimensions of the beam, given in Table 5.1, are too large to resolve the whole mesostructure of the beam in detail and therefore an embedding approach is used. However, for an embedding approach, the area in which nonlinear effects are expected has to be estimated beforehand. As a consequence, a stress concentrator is introduced in the middle of the beam. To not only affect a certain part of the mesostructure, but also the area of the stress concentration should not be too small and the concentrator has been realized as a circular cutout as depicted in Figure 5.10.

The symmetry plane of the C-profile lies in the x,y-plane. Even though the braid topology is not symmetric with respect to the x,y-plane, the influence of enforcing a symmetric solution is expected to be small and a z-symmetry condition is used. In order to further save computational effort, only the section between the two load application points is regarded. Because of that, the numerical model is loaded by a rotation of $\varphi = \pm 5°$ at the load application points, as depicted in Figure 5.11.
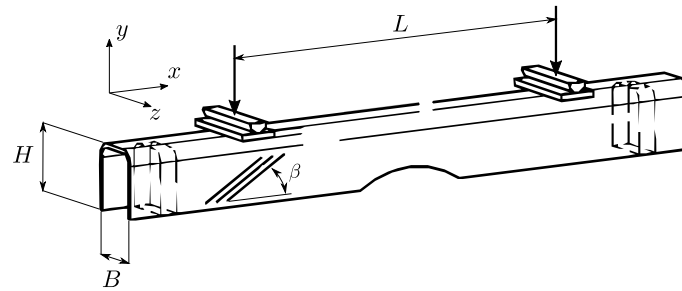
Figure 5.10: C-profile beam specimen under four-point-bending load.

Table 5.1: Dimensions of the beam specimen.

L	H	B	β
400 mm	60 mm	50 mm	30°

Embedding approach.   The detailed braid geometry is resolved in the region around the stress concentrator to capture the complex stress and strain field of the fabric. The aim is that the material nonlinearities take place inside the embedded region and the embedding region can be modeled with linear elastic material. Consequently, the obtained results are only valid as long as the nonlinear effects occur inside the detailed region. To be able to estimate the size of the region of the initial nonlinear material behavior, previous linear-elastic calculations have been conducted that predicted the stress field inside the fabric structure. The resulting size of the embedded region is 58.8 mm by 19.5 mm, which is shown in Figure 5.11.

The embedded region is coupled to the homogenized model using a node-to-surface coupling. Due to the fact, that the level of resolution differs in the two domains, the coupling locally leads to spurious stress concentrations. To alleviate the possibility of such stress concentrations triggering nonlinear effects, the latter are suppressed in the vicinity of the coupling.

Detailed braid model.   Even after applying the embedding approach, the embedded region is still so large, that modeling it with 3D-continuum elements is unfeasible. In order to circumvent this, the shell modeling approach developed in [13] is employed, which exploits the characteristic dimensions of typical braid or weave structures. These structures typically have low thickness-to-width ratios and allow the use of shell elements.
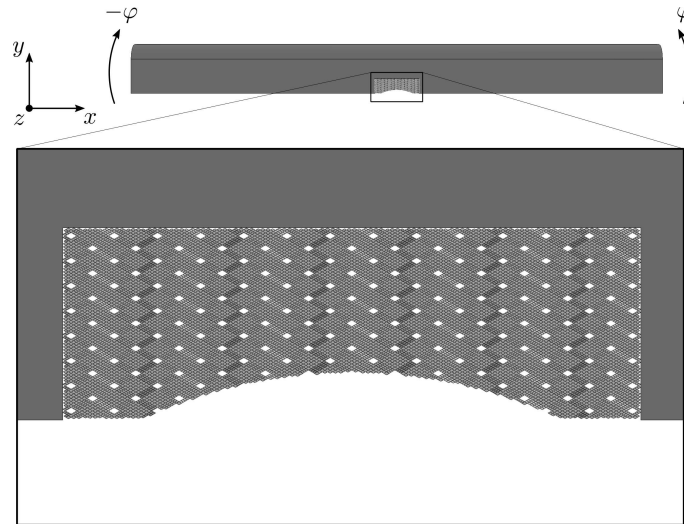
Figure 5.11: C-profile beam with embedding region (top) and detailed embedded region (bottom) with stress concentrator (matrix material is not displayed).

The shell elements condense the three-dimensional nature of the constituents into a surface representation. This leads to a substantial decrease in the required degrees of freedom, while still being able to capture the typical fabric deformation. The model is set up initially with an orthogonal fabric structure where the reference planes of the shells are the midplanes of the tows. The tow geometry is simplified with a rectangular cross-section and a constant thickness along the tow direction. The areas with unreinforced matrix material, also called matrix pockets, are also modeled as shells with reference planes at the top and bottom surface of the unit cell. To fill matrix pockets according to the local geometry, a variable shell thickness is applied. Tie constraints are used to couple the tows with each other and the matrix.

To model a $\pm 30°$ braid, a skewing of the unit cell has to be applied. Since 2D biaxial braids have the same structure as sheared woven fabrics, the strain-free skewing proposed by [17] can be applied. The blunt notch cut out is realized through deleting elements whose centers are inside the cut-out radius.

Tow behavior. Since each tow is only reinforced by fibers in one direction, the constitutive model introduced in the present work is used to model their material behavior. Consequently, the material behavior of the pristine tows is taken to be transversely isotropic and linear elastic. It is assumed that the nonlinearities, that occur at higher loads, are

Table 5.2: Material properties of the matrix material.

E^{M}	ν^{M}	$R_{\mathrm{y}}^{\mathrm{M}}$	R^{M}	$\mathcal{G}^{\mathrm{M}}$
2.89 GPa	0.38	55 MPa	77.8 MPa	500 J/m^2

caused mainly by stiffness degradation and accumulation of unrecoverable strains. Since it is not possible to manufacture specimens with the 88% fiber volume fraction of the tows, the properties of the tows cannot be determined from experiments. In order to get useful input data, the properties are taken from data obtained for UD-plies with a fiber volume fraction of 60% and then scaled to 88%. The resulting material properties are shown in Appendix E in Table E.5 and E.6.

Matrix pocket behavior. The unreinforced matrix pockets are areas of pure resin material. Typical polymeric matrix materials exhibit isotropic behavior in the elastic range and are commonly modeled using an elastic-plastic constitutive law. As most polymers show a pressure-dependent yield behavior, a Drucker-Prager type plasticity model is used. Additionally, the ductile damage model from ABAQUS/Standard 2018 (SIMULIA, Providence, RI, USA) is used to enable the damage to go through the matrix pockets. The material properties are shown in Table 5.2.

Homogeneous ply model. It is assumed that no material nonlinearities occur in the embedding region around the detailed braid model and that the material properties of the braid unit cell can be obtained using conventional homogenization schemes. In the present work, a first order numerical homogenization scheme is used, applying a separation of length scales concept. This requires the characteristic size of the fabric unit cell to be sufficiently smaller than the characteristic size of the macroscopic structure. This requirement is only fulfilled to a certain extent with fabric unit cells and has to be kept in mind during the following analysis. Due to large rotations between the tows, the general effective response of the braid unit cell is nonlinear, even with linear elastic material behavior of the constituents. However, this effect is considered negligible in this work and a linear elastic response of the homogenized fabric ply is assumed. The material properties of each ply can be found in Table 5.3.

Table 5.3: Effective material properties of the homogenized ply.

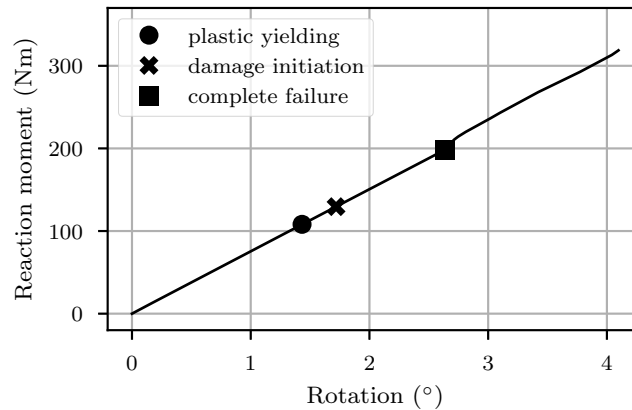| E_1	$E_2 = E_3$	$\nu_{12} = \nu_{13}$	$G_{12} = G_{13} = G_{23}$
44.84 GPa	8.48 GPa	1.61	28.88 GPa

Figure 5.12: Reaction moment-rotation curve at the right load application point. The increments in which the first integration point indicated plastic yielding (circle), damage initiation (cross), and complete failure (square) are shown.

5.3.2 Results

Moment–rotation response. The model predicts a linear moment-rotation curve up to an applied rotation of $\varphi = 4.09°$, as depicted in Figure 5.12. At this point, the simulation stops due to convergence problems of the global Newton solver. Even though the nonlinear mechanisms are not visible in the global moment-rotation response, they initiate early on in the simulation. The plastic yielding of the tows initiates at an applied rotation of $\varphi = 1.43°$, depicted in Figure 5.12. Damage is initiated at an applied angle of $\varphi = 1.71°$, whereas the first integration point completely failed at an applied angle of $\varphi = 2.63°$.

Plastic strains. The plastic yielding in the top ply starts in the bridge between overlapping tow regions, almost in the center of the stress concentrator. The in-plane shear component γ_{12}^{p} of the plastic strain tensor is the most dominant and depicted in Figure 5.13 for the last converged increment. The plastic shear angle in the $+30°$ degree tows is positive, while it is negative in the $-30°$ degree tows. The magnitude reaches 5% close
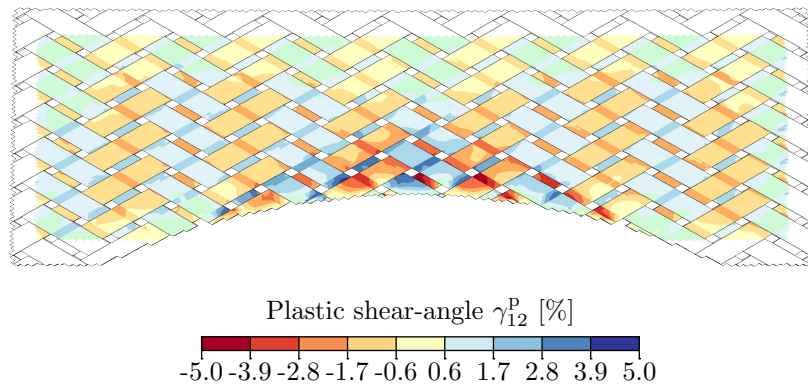
Plastic shear-angle γ_{12}^{p} [%]

-5.0 -3.9 -2.8 -1.7 -0.6 0.6 1.7 2.8 3.9 5.0

Figure 5.13: Plastic in-plane shear angle γ_{12}^{p} in the embedded region in the top ply.

Plastic transverse strain $\varepsilon_{22}^{\mathrm{p}}$ [%]

-0.2 -0.2 -0.1 -0.1 -0.0 0.0 0.1 0.1 0.2 0.2
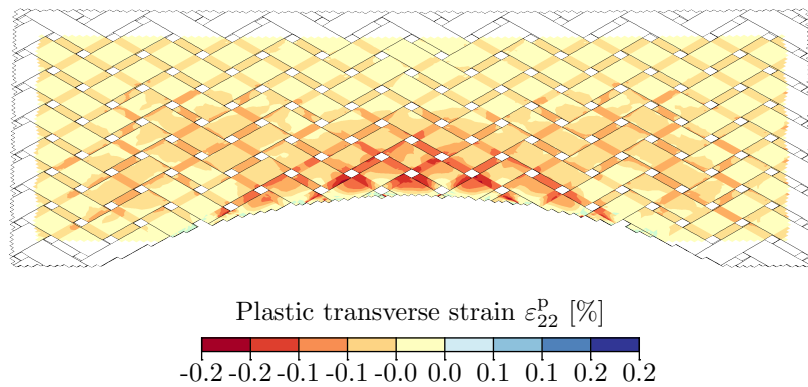
Figure 5.14: Plastic in-plane tarnsverse normal strain $\varepsilon_{22}^{\mathrm{p}}$ in the embedded region in the top ply.

to the edge of the stress concentrator at the bridges between overlapping tow regions. At this stage the size of the embedded region is still large enough to contain the whole plastic region. The plastic strain distribution in the second ply is mirrored by the y,z-plane.

The plastic in-plane transverse normal strain $\varepsilon_{22}^{\mathrm{p}}$, depicted in Figure 5.14, is mostly negative and reaches a magnitude of 2%. It also accumulates in the bridges between the overlapping tow regions. The compressive transverse plastic strains can be explained by the rotation of the tows, which rotate towards the beam axis. As a result, the more compliant bridges between the overlapping tow regions get compressed.

Damage. Only the damage variable d_2 occurs during the simulation. It reaches a value of 1 in small regions in the vicinity of the stress concentrator. The transverse stress σ_2 is negative in the tows in the embedded region. As a result, the tow material can

Damage variable d_2 [-]
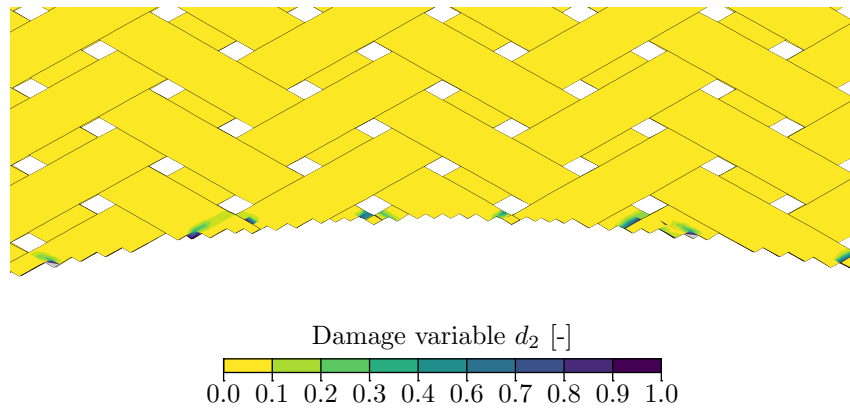
0.0 0.1 0.2 0.3 0.4 0.6 0.7 0.8 0.9 1.0

Figure 5.15: Damage variable d_2 in the embedded region in the top ply.

withstand higher shear stresses according to the Puck failure criterion. This limits the damage evolution in the model and the damage variable d_2 occurs only at the vicinity of the cut-out, as depicted in Figure 5.15.

5.3.3 Discussion

This application presents a modeling approach for the numerical simulation of large scale fabric structures with nonlinear material behavior. The applied embedding approach provides detailed results for the regions of interest while keeping the computational complexity acceptable. The combination of shell modeling for the embedded region with a constitutive model for the damage and plasticity of the tows enables the prediction of ductile mechanisms occurring in the mesostructure of fabric composites. Simulations of a C-profile beam with a blunt notch cutout are presented, that predict large plastic deformations in the tows. This nonlinearity, which cannot be captured on the macroscale, reaffirms the approach to resolve the mesostructure in the model.

The simulation predicts fully damaged material at the blunt notch cutout, which leads to convergence problems. Even though the post softening response cannot be obtained, the model provides information about the softening onset. It is shown that the reaction moment can be increased substantially from the point of initial plastic yielding until the first integration point totally failed. Since hardening plasticity and damage can be tolerated to some extent, this information can be exploited in the design of fabric structures.

In conclusion, the proposed approach gives insights into the nonlinear behavior of

fabric structures and can assist their failure tolerant design. The model is able to predict the plastic yielding and hardening damage, as well as the critical point of softening damage onset.

Chapter 6

Summary

The present work proposes a constitutive model for predicting fiber damage, inter-fiber damage, and plastic yielding in fiber-reinforced polymers. The main contribution is an implicit, effective strength-based damage formulation for inter-fiber damage that can be calibrated according to multiple experimental curves. The stiffness degradation related to the inter-fiber damage variables is formulated by recourse to a micromechanics method. The model uses the Puck failure criterion as a damage condition and employs the principles of equivalent elastic and plastic strain. The damage condition is expressed in terms of effective stresses. As a consequence, the numerical solution procedure is simplified because effective stresses can be calculated explicitly from the strain increment. Due to these measures, the constitutive equations can be solved efficiently such that the model can be used to perform structural computations.

To decouple damage and plasticity, the proposed model uses a Helmholtz free energy potential with independent parts for the elastically-stored and the plastic energy. Additionally, the evolution equations for the plastic internal state variables are formulated by maximizing the effective instead of the nominal plastic dissipation. As a consequence, the plasticity formulation is independent of the damage evolution, which enables a simplified sequential solution scheme.

The prediction of the constitutive model for a $[\pm 45°]^{\mathrm{s}}$-laminate under a tension-compression load cycle is compared to the experimental data. It is shown that the model can be calibrated to accurately predict kinematic hardening behavior, including the stress at which further yielding after reverse loading occurs.

The predictions for an open hole tension test show, that the proposed constitutive model is well suited to model damage and plasticity of FRPs in structural computations. The computational robustness and efficiency of the solution algorithm enable acceptable computation times even for large numerical models.

Appendix A

Auxiliary matrices

Table A.1: General auxiliary matrices for the calculation of the algorithmic consistent material tangent matrix.

$$\mathrm{L}^{\sigma} = \left(\Delta\lambda_p \frac{\partial^2 F_p\left(\tilde{\boldsymbol{\sigma}}, \tilde{\mathbf{A}}\right)}{\partial \tilde{\boldsymbol{\sigma}}^2} + \mathbb{C}_0 \right) \mathbb{M}(\mathbf{d}^{\mathrm{v}}) \tag{A.1}$$

$$\mathrm{L}^{\sigma,\mathrm{P}} = \left(\Delta\lambda_p \frac{\partial^2 F_p\left(\tilde{\boldsymbol{\sigma}}, \tilde{\mathbf{A}}\right)}{\partial \tilde{\boldsymbol{\sigma}} \partial \tilde{\mathbf{A}}} \frac{\mathrm{d}\tilde{\mathbf{A}}(\mathbf{a})}{\mathrm{d}\mathbf{a}} \quad \frac{\partial F_p\left(\tilde{\boldsymbol{\sigma}}, \tilde{\mathbf{A}}\right)}{\partial \tilde{\boldsymbol{\sigma}}} \right) \tag{A.2}$$

$$\mathrm{L}^{\sigma,\mathrm{M}} = \left(0 \quad \left(\Delta\lambda_p \frac{\partial^2 F_p\left(\tilde{\boldsymbol{\sigma}}, \tilde{\mathbf{A}}\right)}{\partial \tilde{\boldsymbol{\sigma}}^2} \frac{\mathrm{d}\mathbb{M}(\mathbf{d}^{\mathrm{v}})}{\mathrm{d}\mathbf{d}^{\mathrm{m,\ v}}} \boldsymbol{\sigma} + \mathbb{C}_0 \frac{\mathrm{d}\mathbb{M}(\mathbf{d}^{\mathrm{v}})}{\mathrm{d}\mathbf{d}^{\mathrm{m,\ v}}} \left(\boldsymbol{\sigma} - \boldsymbol{\sigma}_n \right) \right) \quad 0 \right) \tag{A.3}$$

$$\mathrm{L}^{\sigma,\mathrm{F}} = \left(\Delta\lambda_p \frac{\partial^2 F_p\left(\tilde{\boldsymbol{\sigma}}, \tilde{\mathbf{A}}\right)}{\partial \tilde{\boldsymbol{\sigma}}^2} \frac{\mathrm{d}\mathbb{M}(\mathbf{d}^{\mathrm{v}})}{\mathrm{d}d_1^{\mathrm{y}}} \boldsymbol{\sigma} + \mathbb{C}_0 \frac{\mathrm{d}\mathbb{M}(\mathbf{d}^{\mathrm{v}})}{\mathrm{d}d_1^{\mathrm{y}}} \left(\boldsymbol{\sigma} - \boldsymbol{\sigma}_n \right) \right) \tag{A.4}$$

Table A.2: Auxiliary parameters for fiber damage the calculation of the algorithmic consistent material tangent matrix.

$$\mathrm{L}^{\mathrm{F}} = 1 + \frac{\Delta t}{\eta} \tag{A.5}$$

$$\mathrm{L}^{\mathrm{F},\varepsilon} = \frac{\Delta t}{\eta} \frac{\mathrm{d}d_1(\varepsilon_1)}{\mathrm{d}\varepsilon_1} \tag{A.6}$$

$$\tag{A.7}$$

Table A.3: Auxiliary matrices for plastic yielding for the calculation of the algorithmic consistent material tangent matrix.

$$
\mathrm{L}^{\mathrm{P},\sigma} = \begin{pmatrix} \Delta\lambda_p \dfrac{\partial^2 F_p(\tilde{\boldsymbol{\sigma}},\tilde{\mathbf{A}})}{\partial\tilde{\mathbf{A}}\partial\tilde{\boldsymbol{\sigma}}}\mathbb{M}(\mathbf{d}^{\mathrm{v}}) \\[2ex] \dfrac{\partial}{\partial\tilde{\boldsymbol{\sigma}}}F_p\left(\tilde{\boldsymbol{\sigma}},\tilde{\mathbf{A}}\right)\mathbb{M}(\mathbf{d}^{\mathrm{v}}) \end{pmatrix} \tag{A.8}
$$

$$
\mathrm{L}^{\mathrm{P}} = \begin{pmatrix} \Delta\lambda_p \dfrac{\partial^2 F_p(\tilde{\boldsymbol{\sigma}},\tilde{\mathbf{A}})}{\partial\tilde{\mathbf{A}}^2}\dfrac{\mathrm{d}\tilde{\mathbf{A}}(\mathbf{a})}{\mathrm{d}\mathbf{a}}+\mathbf{1} & \dfrac{\partial F_p(\tilde{\boldsymbol{\sigma}},\tilde{\mathbf{A}})}{\partial\tilde{\mathbf{A}}} \\[2ex] \dfrac{\partial F_p(\tilde{\boldsymbol{\sigma}},\tilde{\mathbf{A}})}{\partial\tilde{\mathbf{A}}}\dfrac{\mathrm{d}\tilde{\mathbf{A}}(\mathbf{a})}{\mathrm{d}\mathbf{a}} & 0 \end{pmatrix} \tag{A.9}
$$

$$
\mathrm{L}^{\mathrm{P},\mathrm{M}} = \begin{pmatrix} 0 & \Delta\lambda_p \dfrac{\partial^2 F_p(\tilde{\boldsymbol{\sigma}},\tilde{\mathbf{A}})}{\partial\tilde{\mathbf{A}}\partial\tilde{\boldsymbol{\sigma}}}\dfrac{\mathrm{d}\mathbb{M}(\mathbf{d}^{\mathrm{v}})}{\mathrm{d}\mathbf{d}^{\mathrm{m,\ v}}}\boldsymbol{\sigma} & 0 \\[2ex] 0 & \dfrac{\partial F_p(\tilde{\boldsymbol{\sigma}},\tilde{\mathbf{A}})}{\partial\tilde{\boldsymbol{\sigma}}}\dfrac{\mathrm{d}\mathbb{M}(\mathbf{d}^{\mathrm{v}})}{\mathrm{d}\mathbf{d}^{\mathrm{m,\ v}}}\boldsymbol{\sigma} & 0 \end{pmatrix} \tag{A.10}
$$

$$
\mathrm{L}^{\mathrm{P},\mathrm{F}} = \begin{pmatrix} \Delta\lambda_p \dfrac{\partial^2 F_p(\tilde{\boldsymbol{\sigma}},\tilde{\mathbf{A}})}{\partial\tilde{\mathbf{A}}\partial\tilde{\boldsymbol{\sigma}}}\dfrac{\mathrm{d}\mathbb{M}(\mathbf{d}^{\mathrm{v}})}{\mathrm{d}d_1^{\mathrm{v}}}\boldsymbol{\sigma} \\[2ex] \dfrac{\partial F_p(\tilde{\boldsymbol{\sigma}},\tilde{\mathbf{A}})}{\partial\tilde{\boldsymbol{\sigma}}}\dfrac{\mathrm{d}\mathbb{M}(\mathbf{d}^{\mathrm{v}})}{\mathrm{d}d_1^{\mathrm{v}}}\boldsymbol{\sigma} \end{pmatrix} \tag{A.11}
$$

Table A.4: Auxiliary matrices for inter-fiber damage for the calculation of the algorithmic consistent material tangent matrix.

$$
\mathrm{L}^{\mathrm{M},\sigma} = \begin{pmatrix} 0 \\[1ex] 0 \\[1ex] \dfrac{\partial}{\partial\tilde{\boldsymbol{\sigma}}}\mathrm{F}_{\mathrm{d}}\left(\tilde{\boldsymbol{\sigma}},\tilde{\mathbf{R}}\right)\mathbb{M}(\mathbf{d}^{\mathrm{v}}) \end{pmatrix} \tag{A.12}
$$

$$
\mathrm{L}^{\mathrm{M}} = \begin{pmatrix} \mathbf{1} & 0 & -\mathbf{D} \\[1ex] -\dfrac{\Delta t}{\eta} & 1+\dfrac{\Delta t}{\eta} & 0 \\[1ex] \dfrac{\partial \mathrm{F}_{\mathrm{d}}(\tilde{\boldsymbol{\sigma}},\tilde{\mathbf{R}})}{\partial\tilde{\mathbf{R}}}\dfrac{\mathrm{d}\tilde{\mathbf{R}}(\mathbf{d})}{\mathrm{d}\mathbf{d}^{\mathrm{m,\ v}}} & \dfrac{\partial \mathrm{F}_{\mathrm{d}}(\tilde{\boldsymbol{\sigma}},\tilde{\mathbf{R}})}{\partial\tilde{\boldsymbol{\sigma}}}\dfrac{\mathrm{d}\mathbb{M}(\mathbf{d}^{\mathrm{v}})}{\mathrm{d}\mathbf{d}^{\mathrm{m,\ v}}}\boldsymbol{\sigma} & 0 \end{pmatrix} \tag{A.13}
$$

$$
\mathrm{L}^{\mathrm{M},\mathrm{F}} = \begin{pmatrix} 0 \\[1ex] 0 \\[1ex] \dfrac{\partial \mathrm{F}_{\mathrm{d}}(\tilde{\boldsymbol{\sigma}},\tilde{\mathbf{R}})}{\partial\tilde{\boldsymbol{\sigma}}}\dfrac{\mathrm{d}\mathbb{M}(\mathbf{d}^{\mathrm{v}})}{\mathrm{d}d_1^{\mathrm{v}}}\boldsymbol{\sigma} \end{pmatrix} \tag{A.14}
$$

Appendix B

Voigt-Nye notation

The treatment of higher order tensors entails certain challenges. First of all, it is not possible to simply represent tensors with an order higher than 2 on paper. But more importantly, higher-order tensors can lead to inefficient implementations. Computer memory is a linear sequence of memory locations and higher order tensors has to be mapped to some kind of linear representation to fit that structure. The lower the tensor order, the simpler the mapping. Additionally, the tensors that are used in the present work show several symmetries and have zero entries in certain positions, which can lead to redundant computations when the full order of the tensor is used.

The use of the Voigt-Nye notation speeds up the computations and simplifies the representation of higher-order tensors. The Voigt-Nye notation makes use of the symmetry of the stress and the strain tensor

$$\boldsymbol{\sigma} = \begin{pmatrix} \sigma_{11} \\ \sigma_{22} \\ \sigma_{33} \\ \sigma_{12} \\ \sigma_{13} \\ \sigma_{23} \end{pmatrix}, \qquad \boldsymbol{\varepsilon} = \begin{pmatrix} \varepsilon_{11} \\ \varepsilon_{22} \\ \varepsilon_{33} \\ 2\varepsilon_{12} \\ 2\varepsilon_{13} \\ 2\varepsilon_{23} \end{pmatrix} \tag{B.1}$$

and represents them as vectors in a 6-dimensional space. It is to be noted that the entries for the strain components with mixed indices $i \neq j$ are equal to the shear-angles $\gamma_{ij} = 2\varepsilon_{ij}$.

Appendix C

Plane stress

For a plane stress state it is assumed that the stress components $\sigma_3 = \sigma_5 = \sigma_6 = 0$. With this assumption, the constitutive equations can be simplified. The fact that $\sigma_3 = 0$, can be used to express $\varepsilon_3^{\mathrm{e}}$ as a function of $\varepsilon_1^{\mathrm{e}}$ and $\varepsilon_2^{\mathrm{e}}$ through the relation

$$\varepsilon_3^{\mathrm{e}} = \frac{\mathbb{C}_{3\alpha}\left(\mathbf{d}\right)\mathbb{C}_{\alpha 1}^{-1}\left(\mathbf{d}\right)}{1 - \mathbb{C}_{3\gamma}\left(\mathbf{d}\right)\mathbb{C}_{\gamma 3}^{-1}\left(\mathbf{d}\right)}\varepsilon_1^{\mathrm{e}} + \frac{\mathbb{C}_{3\beta}\left(\mathbf{d}\right)\mathbb{C}_{\beta 2}^{-1}\left(\mathbf{d}\right)}{1 - \mathbb{C}_{3\gamma}\left(\mathbf{d}\right)\mathbb{C}_{\gamma 3}^{-1}\left(\mathbf{d}\right)}\varepsilon_2^{\mathrm{e}} \ , \tag{C.1}$$

where the Einstein summation notation is used and the indices α, β, γ range form 1 to 2. The fact that $\sigma_5 = \sigma_6 = 0$ in combination with the assumption of an orthotropic material behavior leads to

$$\gamma_5^{\mathrm{e}} = \gamma_6^{\mathrm{e}} = 0 \ . \tag{C.2}$$

Similiar simplification can be done for the plastic strains. The assumption that the fibers show no plastic yielding, leads to

$$\varepsilon_1^{\mathrm{p}} = 0 \ . \tag{C.3}$$

And the assumption that plastic yielding doesn't lead to a volumetric part of the platic strain tensor, leads to

$$\varepsilon_3^{\mathrm{p}} = -\varepsilon_2^{\mathrm{p}} \ . \tag{C.4}$$

Additionally the out-of-plane plastic shear angles

$$\gamma_5^{\mathrm{p}} = \gamma_6^{\mathrm{p}} = 0 \tag{C.5}$$

are assumed to be zero. All stress and strain components with indices $3, 5, 6$ can either be eliminated or expressed through components with indices $1, 2$. As a result, it suffices to

derive the constitutive equations for the stress and strain components with indices $1, 2, 4$ and calculate the other components from that.

Appendix D

UMAT usage

In the present chapter the usage of the user-subroutine UMAT in combination with the Finite Element solver ABAQUS/Standard 2019 (SIMULIA, Providence, RI, USA) is explained. To use the UMAT, the user has to specify the state variables and the material parameters of the constitutive model. The number of state variables is specified by

```
*Depvar, DELETE=9
9,
```

in the input file. This way the global solver can allocate enough memory to store the state variables for every integration point. Additionally, the element deletion feature can be used with the expression `DELETE=INDEX` to tell the solver which state variables contains the information on whether the element containing the current integration point should be deleted from the mesh. For an element to be deleted, all its integration points have to indicate deletion. To provide the FE solver with the initial values of the internal state variables, the expression

```
*Initial Conditions, type=SOLUTION
ELSET, ε₁ᵖ, ε₂ᵖ, ε₃ᵖ, ã₁, ã₂, d₁ᵛ, d₂ᵛ,
d₃ᵛ,DELETE
```

$$\text{ELSET}, \varepsilon_1^{\mathrm{p}}, \varepsilon_2^{\mathrm{p}}, \varepsilon_3^{\mathrm{p}}, \tilde{a}_1, \tilde{a}_2, d_1^{\mathrm{v}}, d_2^{\mathrm{v}},$$
$$d_3^{\mathrm{v}},\text{DELETE}$$

has to be used. The entry `ELSET` specifies the element set, to which the initial conditions are applied. The entry `DELETE` stands for the element deletion flag, which has to be set to 1.

The material parameters required by the constitutive model are passed to the UMAT by the expression

```
*User Material, constants=39
```
BLANK, BLANK, BLANK, E_1, E_2, G_{12}, G_{23}, ν_{12}

Y_0^{T}, Y_1^{T}, Y_2^{T}, Y_2^{T}, BLANK, BLANK, BLANK, $\mathcal{G}^{\mathrm{M,\ T}}$

Y_0^{C}, Y_1^{C}, Y_2^{C}, $\tilde{Y}_3^{\mathrm{C}}$, $\tilde{a}_2^3$, BLANK, c_1^{p}, $\mathcal{G}^{\mathrm{M,\ C}}$

S_0, S_1, S_2, $\tilde{S}_3$, $\tilde{a}_3^3$, BLANK, c_2^{p}, $\mathcal{G}^{\mathrm{M,\ S}}$

X^{T}, X^{C}, $\mathcal{G}^{\mathrm{F,\ T}}$, $\mathcal{G}^{\mathrm{F,\ C}}$, α, p^{T}, p^{C}, η

in the input file. The first three entries are reserved for debugging. The following entries in the first line are elastic constants. The second line consists of parameters for the transverse tensile behavior, the third for the transverse compressive behavior and the fourth line for the in-plane shear behavior. The fifth line consists of parameters for fiber damage, plasticity, the damage condition and the viscous regularization.

Appendix E

Material parameters

E.1 Material system Cycom977-2-35/40-12KHTS-134-300

Table E.1: Elastic properties of a ply for the material system Cycom977-2-35/40-12KHTS-134-300 with a fiber volume fraction of 60%.

E_1	E_2	G_{12}	G_{23}	ν_{12}
(MPa)	(MPa)	(MPa)	(MPa)	(−)
146000	9000	4270	2800	0.34

Table E.2: Parameters for fiber damage of a ply for the material system Cycom977-2-35/40-12KHTS-134-300 with a fiber volume fraction of 60%.

X^{T}	X^{C}	$\mathcal{G}^{\mathrm{F,\ T}}$	$\mathcal{G}^{\mathrm{F,\ C}}$
(MPa)	(MPa)	(N/mm)	(N/mm)
2100	1407	89.8	78.3

Table E.3: Parameters for inter-fiber damage of a ply for the material system Cycom977-2-35/40-12KHTS-134-300 with a fiber volume fraction of 60%.

Y_0^{T}	Y_1^{T}	Y_2^{T}	$\tilde{Y}_3^{\mathrm{T}}$
(MPa)	(MPa)	(MPa)	(MPa)
82	82	85	85.5
Y_0^{C}	Y_1^{C}	Y_2^{C}	$\tilde{Y}_3^{\mathrm{C}}$
(MPa)	(MPa)	(MPa)	(MPa)
96.9	110	220	224
S_0	S_1	S_2	$\tilde{S}_3$
(MPa)	(MPa)	(MPa)	(MPa)
52.5	70	110	112
$\mathcal{G}^{\mathrm{M,\ T}}$	$\mathcal{G}^{\mathrm{M,\ C}}$	$\mathcal{G}^{\mathrm{M,\ S}}$	
(N/mm)	(N/mm)	(N/mm)	
0.2	0.8	1.0	

Table E.4: Miscellaneous parameters of a ply for the material system Cycom977-2-35/40-12KHTS-134-300 with a fiber volume fraction of 60%.

c_1^{p}	c_2^{p}	p^{T}	p^{C}	η
(−)	(−)	(−)	(−)	(s)
20	40	0.3	0.35	2.E−5

E.2 Tow material of the fabric laminated structure

Table E.5: Elastic properties of a ply for the tow material of the fabric laminated structure with a fiber volume fraction of 88%.

E_1	E_2	G_{12}	G_{23}	ν_{12}
(MPa)	(MPa)	(MPa)	(MPa)	(−)
203200	11990	5610	3571	0.22

Table E.6: Parameters for fiber damage of a ply for the tow material of the fabric laminated structure with a fiber volume fraction of 88%.

X^T	X^C	$\mathcal{G}^\mathrm{F,\ T}$	$\mathcal{G}^\mathrm{F,\ C}$
(MPa)	(MPa)	(N/mm)	(N/mm)
2971	1400	114	99.86

Table E.7: Parameters for inter-fiber damage of a ply for the tow material of the fabric laminated structure with a fiber volume fraction of 88%.

Y_0^T	Y_1^T	Y_2^T	$\tilde{Y}_3^\mathrm{T}$
(MPa)	(MPa)	(MPa)	(MPa)
33	33	35	35.05
Y_0^C	Y_1^C	Y_2^C	$\tilde{Y}_3^\mathrm{C}$
(MPa)	(MPa)	(MPa)	(MPa)
70	90	182	184
S_0	S_1	S_2	$\tilde{S}_3$
(MPa)	(MPa)	(MPa)	(MPa)
40	55	74	77
$\mathcal{G}^\mathrm{M,\ T}$	$\mathcal{G}^\mathrm{M,\ C}$	$\mathcal{G}^\mathrm{M,\ S}$	
(N/mm)	(N/mm)	(N/mm)	
0.2	0.8	1.0	

Table E.8: Miscellaneous parameters of a ply for the tow material of the fabric laminated structure with a fiber volume fraction of 88%.

c_1^p	c_2^p	p^T	p^C	η
(−)	(−)	(−)	(−)	(s)
75	10	0.3	0.35	1.E−5

Bibliography

[1] `https://tougetuning.com/wp-content/uploads/2017/03/hd15sbimp-oe-wf-01.jpg`, 2020.

[2] G. I. Barenblatt. The mathematical theory of equilibrium cracks in brittle fracture. In *Advances in applied mechanics*, volume 7, pages 55–129. Elsevier, 1962.

[3] Z. P. Bažant and B. H. Oh. Crack band theory for fracture of concrete. *Matériaux et construction*, 16(3):155–177, 1983.

[4] T. Belytschko and T. Black. Elastic crack growth in finite elements with minimal remeshing. *International journal for numerical methods in engineering*, 45(5):601–620, 1999.

[5] F.-K. Chang, R. A. Scott, and G. S. Springer. Failure of composite laminates containing pin loaded holes—method of solution. *Journal of Composite Materials*, 18(3):255–278, 1984.

[6] C. Chow and T. Lu. On evolution laws of anisotropic damage. *Engineering Fracture Mechanics*, 34(3):679–701, 1989.

[7] D. S. Dugdale. Yielding of steel sheets containing slits. *Journal of the Mechanics and Physics of Solids*, 8(2):100–104, 1960.

[8] S. Dutta and J. C. Kishen. Micromechanical damage model for plain concrete considering propagation of matrix microcracks. *Physical Mesomechanics*, 22(2):96–106, 2019.

[9] T. Flatscher. *A Constitutive Model for the Elasto-Plasto-Damage Ply Behavior in Laminated FRP Composites: Its Development, Implementation, and Application in*

FEM Simulations. PhD thesis, Institut für Leichtbau und Struktur-Biomechanik, TU Wien, 2010.

[10] T. Flatscher and H. Pettermann. A constitutive model for fiber-reinforced polymer plies accounting for plasticity and brittle damage including softening–implementation for implicit fem. *Composite Structures*, 93(9):2241–2249, 2011.

[11] T. Flatscher, C. Schuecker, and H. Pettermann. A constitutive ply model for stiffness degradation and plastic strain accumulation: Its application to the third world wide failure exercise (part a). *Journal of Composite Materials*, 47(20-21):2575–2593, 2013.

[12] T. Flatscher, M. Wolfahrt, G. Pinter, and H. Pettermann. Simulations and experiments of open hole tension tests–assessment of intra-ply plasticity, damage, and localization. *Composites science and technology*, 72(10):1090–1095, 2012.

[13] J. Gager and H. Pettermann. Fem modeling of multilayered textile composites based on shell elements. *Composites Part B: Engineering*, 77:46–51, 2015.

[14] A. Galehdar, W. S. Rowe, K. Ghorbani, P. J. Callus, S. John, and C. H. Wang. The effect of ply orientation on the performance of antennas in or on carbon fiber composites. *Progress In Electromagnetics Research*, 116:123–136, 2011.

[15] A. Gavazzi and D. Lagoudas. On the numerical evaluation of eshelby's tensor and its application to elastoplastic fibrous composites. *Computational mechanics*, 7(1):13–19, 1990.

[16] S. Govindjee, G. J. Kay, and J. C. Simo. Anisotropic modelling and numerical simulation of brittle damage in concrete. *International journal for numerical methods in engineering*, 38(21):3611–3633, 1995.

[17] D. Goyal. *Analysis of 2x2 braided composites.* PhD thesis, Texas A&M University, 2004.

[18] J. Hund, C. Leppin, T. Böhlke, and J. Rothe. Stress-strain characterization and damage modeling of glass-fiber-reinforced polymer composites with vinylester matrix. *Journal of Composite Materials*, 51(4):547–562, 2017.

[19] A. Ibrahimbegovic, P. Jehel, and L. Davenne. Coupled damage-plasticity constitutive model and direct stress interpolation. *Computational Mechanics*, 42(1):1–11, 2008.

[20] W.-G. Jiang, S. R. Hallett, B. G. Green, and M. R. Wisnom. A concise interface constitutive law for analysis of delamination and splitting in composite materials and its application to scaled notched tensile specimens. *International journal for numerical methods in engineering*, 69(9):1982–1995, 2007.

[21] M. Jirásek and J. Zeman. Localization study of a regularized variational damage model. *International Journal of Solids and Structures*, 69:131–151, 2015.

[22] L. M. Kachanov. Time of the rupture process under creep conditions, izy akad. *Nank SSR Otd Tech Nauk*, 8:26–31, 1958.

[23] M. Kachanov. Elastic solids with many cracks and related problems. In *Advances in applied mechanics*, volume 30, pages 259–445. Elsevier, 1993.

[24] S. Kanaun. Effective elastic properties of the medium with an array of thin inclusions. *Revista Mexicana de Fisica*, 39(6):850–869, 1992.

[25] M. Knops. *Analysis of failure in fiber polymer laminates: the theory of Alfred Puck.* Springer Science & Business Media, 2008.

[26] P. Ladeveze and E. LeDantec. Damage modelling of the elementary ply for laminated composites. *Composites science and technology*, 43(3):257–267, 1992.

[27] I. Lapczyk and J. A. Hurtado. Progressive damage modeling in fiber-reinforced materials. *Composites Part A: Applied Science and Manufacturing*, 38(11):2333–2341, 2007.

[28] P. Maimí, P. P. Camanho, J. Mayugo, and C. Dávila. A continuum damage model for composite laminates: Part i–constitutive model. *Mechanics of Materials*, 39(10):897–908, 2007.

[29] A. Matzenmiller, J. Lubliner, and R. Taylor. A constitutive model for anisotropic damage in fiber-composites. *Mechanics of materials*, 20(2):125–152, 1995.

[30] J. Mulhern, T. Rogers, and A. J. M. Spencer. A continuum model for fibre-reinforced plastic materials. *Proc. R. Soc. Lond. A*, 301(1467):473–492, 1967.

[31] S. Murakami. *Continuum damage mechanics: a continuum mechanics approach to the analysis of damage and fracture*, volume 185. Springer Science & Business Media, 2012.

[32] S. G. Nagaraja, M. Pletz, and C. Schuecker. Constitutive modeling of anisotropic plasticity with application to fiber-reinforced composites. *International Journal of Solids and Structures*, 180:84–96, 2019.

[33] S. T. Pinho, C. G. Dávila, P. P. Camanho, L. Iannucci, and P. Robinson. Failure models and criteria for frp under in-plane or three-dimensional stress states including shear non-linearity. 2005.

[34] A. Puck. *Festigkeitsanalyse von Faser-Matrix-Laminaten: Modelle für die Praxis.* Hanser, 1996.

[35] A. Quintanas-Corominas, P. Maimí, E. Casoni, A. Turon, J. A. Mayugo, G. Guil-lamet, and M. Vázquez. A 3d transversally isotropic constitutive model for advanced composites implemented in a high performance computing code. *European Journal of Mechanics-A/Solids*, 71:278–291, 2018.

[36] J. Reinoso, G. Catalanotti, A. Blázquez, P. Areias, P. Camanho, and F. París. A consistent anisotropic damage model for laminated fiber-reinforced composites using the 3d-version of the puck failure criterion. *International Journal of Solids and Structures*, 126:37–53, 2017.

[37] C. Schuecker and H. E. Pettermann. A continuum damage model for fiber reinforced laminates based on ply failure mechanisms. *Composite structures*, 76(1-2):162–173, 2006.

[38] M. Schwab and H. Pettermann. Modelling and simulation of damage and failure in large composite components subjected to impact loads. *Composite Structures*, 158:208–216, 2016.

[39] C. V. Singh and R. Talreja. A synergistic damage mechanics approach to mechanical response of composite laminates with ply cracks. *Journal of Composite Materials*, 47(20-21):2475–2501, 2013.

[40] C. Sun and J. Chen. A simple flow rule for characterizing nonlinear behavior of fiber composites. *Journal of Composite Materials*, 23(10):1009–1020, 1989.

[41] F. Van der Meer and L. Sluys. A phantom node formulation with mixed mode cohesive law for splitting in laminates. *International Journal of Fracture*, 158(2):107, 2009.

[42] M. Vogler, R. Rolfes, and P. Camanho. Modeling the inelastic deformation and fracture of polymer composites–part i: plasticity model. *Mechanics of Materials*, 59:50–64, 2013.

[43] W. Voigt et al. *Lehrbuch der Kristallphysik*, volume 962. Teubner Leipzig, 1928.

[44] K. V. Williams, R. Vaziri, and A. Poursartip. A physically based continuum damage mechanics model for thin laminated composite structures. *International Journal of Solids and Structures*, 40(9):2267–2300, 2003.

[45] J.-Y. Wu and M. Cervera. A thermodynamically consistent plastic-damage framework for localized failure in quasi-brittle solids: Material model and strain localization analysis. *International Journal of Solids and Structures*, 88:227–247, 2016.